Bulletin of the Geological Society of Finland, Vol. 95, 2023, pp 5–32 https://doi.org/10.17741/bgsf/95.1.001

Multiscale mapping and scaling analysis of the censored brittle structural framework within the crystalline bedrock of southern Finland

VERTAISARVIOITU
KOLLEGIALT GRANSKAD
PEER-REVIEWED
www.tsv.fi/tunnus

Nicklas Nordbäck[1,2*], Nikolas Ovaskainen[1,2], Mira Markovaara-Koivisto[1], Pietari Skyttä[2], Antti Ojala[2], Jon Engström[1] and Casey Nixon[3]

[1]*Geological Survey of Finland, Vuorimiehentie 5, FI-02151, Espoo, Finland*
[2]*Department of Geography and Geology, University of Turku, Akatemiankatu 1, FI-20014, Turku, Finland*
[3]*Department of Earth Science, University of Bergen, P.O. Box 7803, N-5020, Bergen, Norway*

Abstract

Fracture studies commonly lack data for the length range between 10 m to 1 km. For this reason, scaling laws are required to extrapolate fracture properties, for example in discrete fracture network models. This study focused on analysis and correlation of topology, orientation and length distribution of multiscale fracture datasets to assess their scalability. The used datasets comprise UAV-derived photogrammetric models from natural outcrops and lineaments mapped using airborne LiDAR, bathymetry and aerogeophysical data, in several contrasting scales and resolutions.

This study highlights challenges in acquiring uncensored and coherent brittle structural datasets from source data characterized by a large span of resolutions between the remote sensing datasets and models of the fractured outcrop. In specific, collected data was found to be potentially biased and affected by uncertainties related to both the censoring by sedimentary cover and the scale of observation.

Our results revealed differences between lineament and outcrop fracture orientations, as well as difficulties in assessing topological parameters from lineament datasets. The 1:200 000 resolution was found best suited to the mapping of lineament length and resulted in a length distribution power law exponent of -1.92. For outcrop fractures that are less than 2 m long, the lognormal length distribution provided the only good fit to our data, while the longer outcrop fractures fitted relatively well with a power law exponent of -2.26.

Keywords: remote sensing, lineament, fracture network, length distribution, orientation, topology

*Corresponding author (email nicklas.nordback@gtk.fi)

Editorial handling: Arto Luttinen (email: arto.luttinen@helsinki.fi)

1. Introduction

Brittle structures, such as faults and other fractures (e.g. veins and joints), affect the stability and geomechanical parameters of rock volumes (e.g. Barton et al. 1974; Hoek & Brown, 1980; Hudson et al. 2011) and may act as pathways for fluid flow (e.g. Brace 1980; Barton et al. 1995; Zimmerman & Main 2004; Bense et al. 2013). Consequently, brittle structures play a key role in the suitability of bedrock volumes for different underground applications, including construction, energy and mining. The growing need for the utilization of bedrock volumes places challenges on both sustainable spatial planning (Evans et al. 2009) and the assessment of associated risks. As a result, the availability of reliable data for fracture characterization, stress state modelling and hydrogeological models has become essential. Since each individual fracture within a fractured rock mass cannot be deterministically modelled, discrete fracture network (DFN) models are used for further analysis of the bedrock behavior. DFN models are based on statistical distributions and parameter relationships of the sampled fracture datasets. However, the characterisation of a 3D-fracture network is associated with challenges related to the accurate quantification of i) fracture lengths and geometries, ii) fracture apertures (Nordqvist et al. 1992; Mi et al. 2014; Huang et al. 2019), and iii) topological relationships between fractures (Manzocchi 2002; Sanderson & Nixon, 2015). These properties not only characterize the fracture network, but also the permeability of the rock mass (Sanderson & Nixon, 2018).

Geological datasets associated with brittle deformation structures within the upper parts of the crust often remain incomplete due to limitations such as i) the lack of availability of representative outcrops above the 10 m scale range, ii) low resolution geophysical and remote sensing data and iii) inherent dimensional restrictions (e.g. one-dimensional drillhole data and two-dimensional outcrop data). Within glaciated shield areas, such as the Precambrian crystalline bedrock of Finland, direct observations are primarily limited by the absence, or limited size, of outcrops. For this reason, particularly the larger brittle features, such as fault zones, are represented by linear sediment-covered topographic depressions (O'Leary et al. 1976; Meixner et al. 2018) and only rarely available for direct field observations. On the other hand, the unweathered surfaces are ideal for observation of smaller brittle features, such as joints, in higher resolutions.

To manage the above limitations, scaling laws are used (Dichiarante et al. 2020; Ceccato et al. 2022) to interpolate and extrapolate the intensity, length distribution and aperture of fractures into the scales that lack data. Scaling laws provide a better control over length-distributions when datasets are integrated and analysed across multiple scales (e.g. Bonnet et al. 2001; Bertrand et al. 2015; Chabani et al. 2021). However, not all brittle systems are scalable but instead more accurately represented by scale-limited laws such as lognormal (Odling et al. 1999) and exponential (Le Garzic et al. 2011). Nevertheless, even if a scaling law is found to represent a portion of multiscale fracture data, individual brittle systems can have upper and lower limits where scaling laws remain valid (Bonnet 2001; Davy et al. 2010). These boundaries may be caused by: (i) the structural anisotropy of the material, e.g. lithological variation, or (ii) different mechanisms of fracture formation (e.g. extension fractures and faults). In previous studies that combine outcrop and lineament data the absence of large outcrops has caused a major gap in data for structures between 10 m and 1 km long (Fox et al. 2012; Ovaskainen 2020). This causes an uncertainty within the selection of the appropriate scaling law when extrapolating across this gap.

In this study, we aim to i) find the optimal resolutions for investigating brittle structures of different scales, and ii) test the applicability of fracture system scaling laws within complexly deformed crystalline bedrock in southern Finland (Fig. 1). Our approach involves using multiscale datasets from unmanned aerial vehicle (UAV)-derived photogrammetry (two different

resolutions at outcrop-scales) and airborne LiDAR integrated with bathymetric and aerogeophysical data for lineaments (full-resolution, 1:200 000 and 1:500 000 resolution). Here, we focus on the potential scalability of the topology, orientation, and length distribution across these five datasets. In addition, to understand the geological significance of the lineaments, we discuss the relationship between the lineaments mapped in this study and the known lithology and geological structures. Based on our analysis, we propose the 1:200 000 resolution as most suitable for capturing major lineaments (supposedly representing major fault zones) within southern Finland, while the two other lineament resolutions are associated with higher levels of censoring. In addition, we argue that our UAV outcrop datasets are mainly useful for characterizing local joint networks at the outcrop scale. Thereby, this paper offers examples of the benefits and drawbacks of different datasets and highlights uncertainties related to the extrapolation of brittle parameters between different scales.

2. Geological Background

The bedrock of the southern Finland study area (Fig. 1; 1:500 000 scale; study areas and scales summarized in Table 1) was formed and subsequently modified during the prolonged ~1.9–1.8 Ga Svecofennian orogeny (Nironen 1997; Hermansson et al. 2008; Lahtinen et al. 2009; Bogdanova et al. 2015). The bedrock comprises supracrustal and early to late-orogenic intrusive rocks with mafic to felsic compositions (Kara et al. 2021, 2022) and is characterized by an overall high metamorphic grade associated with high-T low-P conditions (Väisänen & Hölttä 1999). The bedrock was subjected to multiple events of distributed deformation during partially overlapping compressional (at 1.89–1.86 Ga; Van Staal & Williams 1983; Torvela et al. 2008; Torvela & Kurhila 2020) to extensional (1.86–1.82 Ga; Lahtinen et al. 2005; Skyttä & Mänttäri 2008) and transpressional stages (1.82–1.80 Ga; Ehlers et al. 1993; Väisänen et al. 2002; Skyttä et al. 2006). The resulted ductile structures are transected by sub-vertical ductile shear zones that form a network of continuous E–W zones and abutting shorter N–S to NE–SW zones (Fig. 2; Väisänen & Hölttä 1999; Väisänen & Skyttä 2007). The oldest of these shear zones were formed at 1.85 Ga (Torvela et al. 2008; Torvela & Kurhila 2022), while the majority were formed as a response to late-orogenic transpression (1.82–1.79 Ga; Väisänen & Skyttä 2007).

Southern Finland has been covered by the Fennoscandian Ice Sheet (FIS) several times during the Late Quaternary (e.g. Donner 1995; Boulton et al. 2001; Palacios et al. 2021) and was last deglaciated between 13 and 10 ka (Ojala et al. 2013; Stroeven et al. 2016). Due to glacial advances, the crystalline bedrock of the Fennoscandian Shield exhibits distinct curvilinear patterns of glacial scouring and erosion (Kleman et al. 2008). The scouring formed under rapid ice flow conditions, generally towards the margins of the FIS (Boulton et al. 2001). Southern Finland is nowadays partially covered by glacial and interglacial sediments. Quaternary deposits are mostly very thin or absent in the Inkoo study area (Fig. 1), and the bedrock outcrops are relatively well exposed.

Transition from ductile to brittle structural regime occurred soon after the Svecofennian orogeny (1.75 Ga and onwards; Mattila & Viola 2014) and was associated with brittle reactivation of existing shear zones (e.g. Heeremans & Wijbrans 1999; Väisänen & Skyttä 2007; Nordbäck et al. 2022) and generation of new brittle deformation zones. Altogether, seven stages of brittle overprint covering a period of 1.75 to 0.9 Ga have been recognized, dominantly from fault-slip data and structurally constrained geochronology work (Mattila & Viola 2014; Nordbäck et al. 2022). By the end of the Mesoproterozoic (1.0 Ga), all the brittle fault systems had already nucleated and any later brittle deformation caused only the reactivation of previous structures (Mattila & Viola 2014).

For generation and localization of the brittle structures, diverse pieces of evidence suggest significant structural inheritances from older

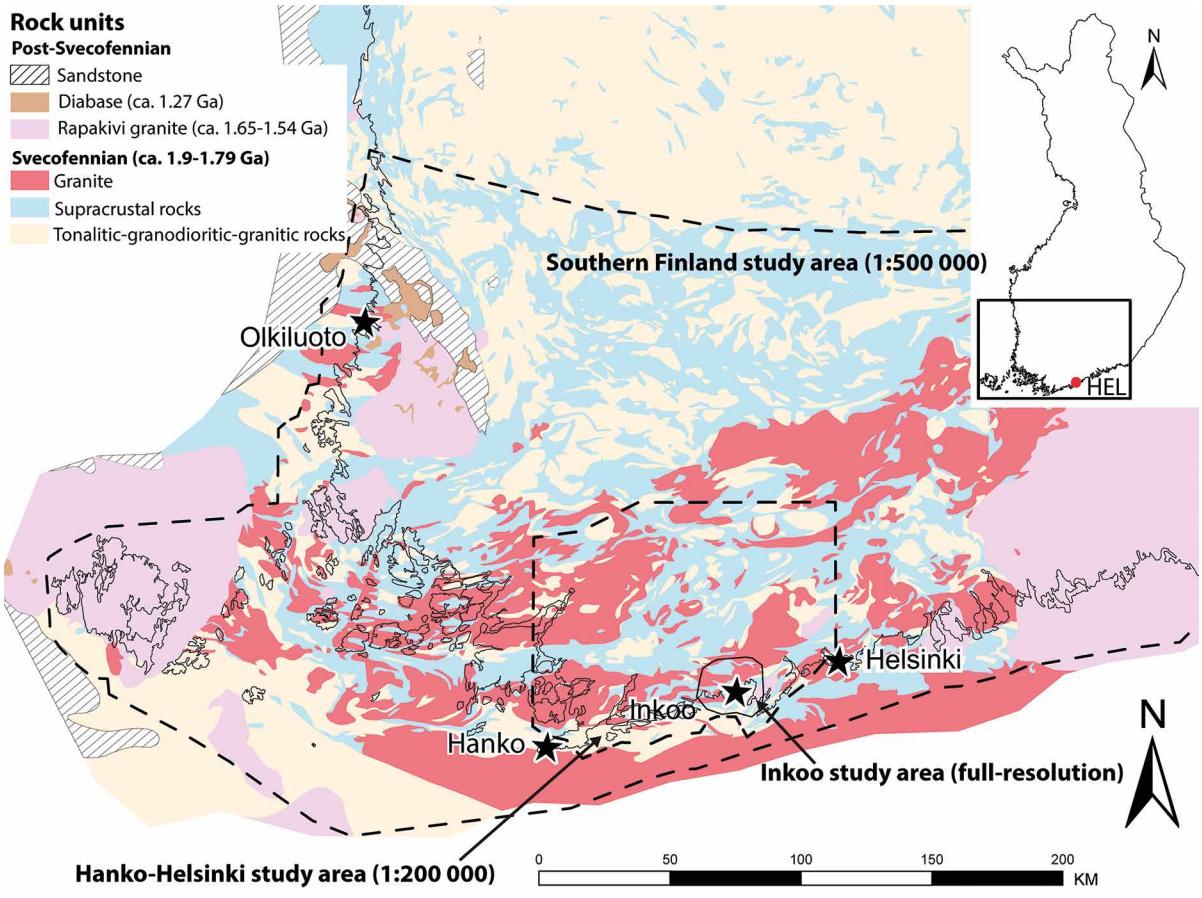

Figure 1. Generalised geological map of south-western Finland. The extent of the lineament study areas is shown by polygons and the locations of Inkoo, Hanko, Helsinki and Olkiluoto with black stars. The figure is based on the Geological Map of Finland – Bedrock 1:1 000 000 © Geological Survey of Finland 2016, modified from Nordbäck et al. 2022.

structures: i) the repeated reactivations of the ductile shear zones (e.g. Heeremans & Wijbrans 1999; Väisänen & Skyttä 2007; Mattila & Viola 2014), ii) ductile shear zones and fault zones acting as intrusion pathways allowing the emplacement of the 1.65–1.47 Ga rapakivi granites and diabase dykes during the Mesoproterozoic extension (Heeremans & Wijbrans 1999; Korja et al. 2001; Rämö & Haapala 2005; Pajunen et al. 2008; Mattila & Viola 2014; Rämö & Mänttäri 2015), and iii) structural and lithological control over the orientation distribution of joints (Wennerström et al. 2008), including the control of early faulting over the density and orientation of the subsequently developed joints (Fig. 1; Skyttä et al. 2021).

The central parts of the Inkoo (full-resolution) study area (Fig. 2) are dominated by migmatized quartz-feldspar gneisses, mica gneisses and amphibolites that on the outcrops display large compositional variations (Laitala 1961; Sakaguchi 2017) and complex deformation structures. By contrast, the widely occurring pegmatitic granites are weakly foliated but frequently contain inclusions of supracrustal gneisses, and foliated synorogenic granodiorites. The south-eastern part of the area is dominated by the anorogenic Obbnäs rapakivi intrusion, and hence more homogeneous in character (Fig. 2). The porphyritic Obbnäs rapakivi granite displays weak magmatic foliation and more intense tectonic foliation attributed

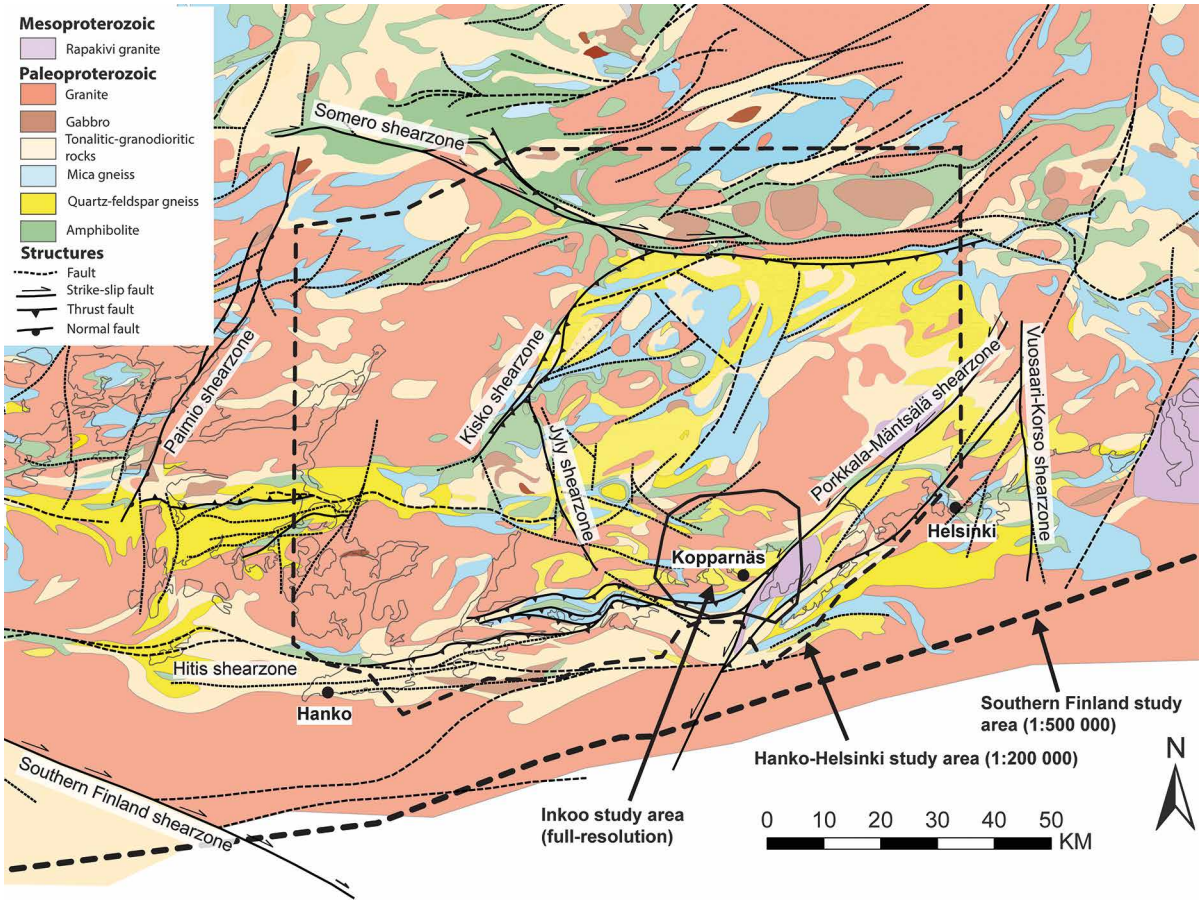

Figure 2. Geological map of the Hanko–Helsinki (1:200 000) study area. Location of previously recognised major ductile shear zones and major faults are indicated on the map. Lithological map and structures based on Bedrock of Finland 1:200 000 geological map © Geological Survey of Finland 2013.

to tectonic activity along the ductile Porkkala–Mäntsälä shear zone (PMSZ; Kosunen 1999) during and after magma crystallisation (1.65 Ga ago; Heeremans & Wijbrans 1999). The E–W trending main foliation within the Inkoo study area is deflected towards a NE–SW trend in the vicinity of PMSZ. For the Helsinki capital area further in the east, a pattern of E–W and ENE–WSW trending ductile shear zones, and NE–SW, N–S and E–W trending fault zones is characteristic (Elminen et al. 2008). Based on available geological maps, a similar pattern can be recognized within the Hanko–Helsinki study area (1:200 000; Fig. 2).

3. Terminology

For the terminology of brittle structures, we follow the definitions by Peacock et al. (2016) and Neuendorf et al. (2011). With *displacement* we refer to the relative movement of bedrock bodies across a discontinuity. We use the term *fracture* to collectively refer to all brittle discontinuities within bedrock, and the term *joint* for fractures that are macroscopically unrelated to any displacement structures. *Fault* is used collectively for the brittle structures with a macroscopically observable displacement. Faults without macroscopically observable *damage zones* are described as *shear*

fractures and faults with damage zones as *fault zones*. Typically, large-scale fault zones include *fault cores* which are narrow high-strain zones that have accommodated the displacement and are associated with the formation of fault rocks. A *damage zone* is the volume of deformed rock around a fault core. We use the term *ductile shear zone* for large-scale zones of localised ductile shear deformation. Since ductile shear zones represent anisotropy and zones of weakness within the bedrock, many ductile shear zones have been reactivated as fault zones within the brittle regime. The term *lineament* is used for linear topographic and geophysical anomalies within the bedrock, which are thought to represent brittle structures. Thus, lineaments are not verified or characterised geological structures and may also be produced by other processes that cannot always be distinguished from lineaments caused by brittle structures, particularly within areas of thick sedimentary cover or human influence (Palmu et al. 2015; Sallasmaa et al. 2016). A *trace* is the line representing a fracture intersecting the plane of observation.

4. Generation of polyline datasets

We generated lineament and fracture trace datasets, as polylines in ArcGIS (© ESRI), from three different lineament scales and two different outcrop scales. The names and extents of the study areas, and associated datasets are summarized in Table 1.

4.1. Lineament mapping

To acquire multiscale lineament datasets (Table 1), we used airborne topographic LiDAR data integrated with bathymetric and aerogeophysical datasets (source data are summarised in Table 2 and visualised in Fig. 3). Using all these datasets, lineaments were mapped at two different resolutions (Fig. 4a,b): the resolution of 1:500 000 (1:500k) for the southern Finland study area and 1:200 000 (1:200k) for the Hanko–Helsinki study area (Fig. 1). A third and more detailed lineament mapping using only LiDAR data, was performed within the Inkoo study area at the full resolution (2 m) of the LiDAR dataset (Fig. 4c).

For topographic lineament mapping we utilized the ground elevation DEM processed at the Geological Survey of Finland from the airborne topographic LiDAR data by the National Land Survey of Finland (with 0.5 points/m^2 with a mean altitude error of 0.3 m). For the visualisation of the LiDAR DEM and highlighting the lineaments, we followed the workflow previously utilised by Palmu et al. (2015). To identify and extend lineaments in areas covered by water, we used the EMODnet Bathymetry Consortium (2018) open-source bathymetric data.

We performed geophysical lineament mapping based on the aerogeophysical magnetic and electromagnetic data provided by the Geological Survey of Finland (see Hautaniemi et al. 2005). Lineaments were separately traced from these maps based on both magnetic minima and maxima and

Table 1. Summary of the study areas and line datasets

Study area	Scale	Data type	Spatial coverage	Number of polylines
Southern Finland	1:500 000	Lineament	90 429 km^2	820
Hanko–Helsinki	1:200 000	Lineament	9 778 km^2	935
Inkoo	Full resolution	Lineament	490 km^2	1 874
Kopparnäs	UAV	Outcrop fracture	1.89 hm^2	12 869
Kopparnäs	Detailed UAV	Outcrop fracture	0.02 hm^2	1 219

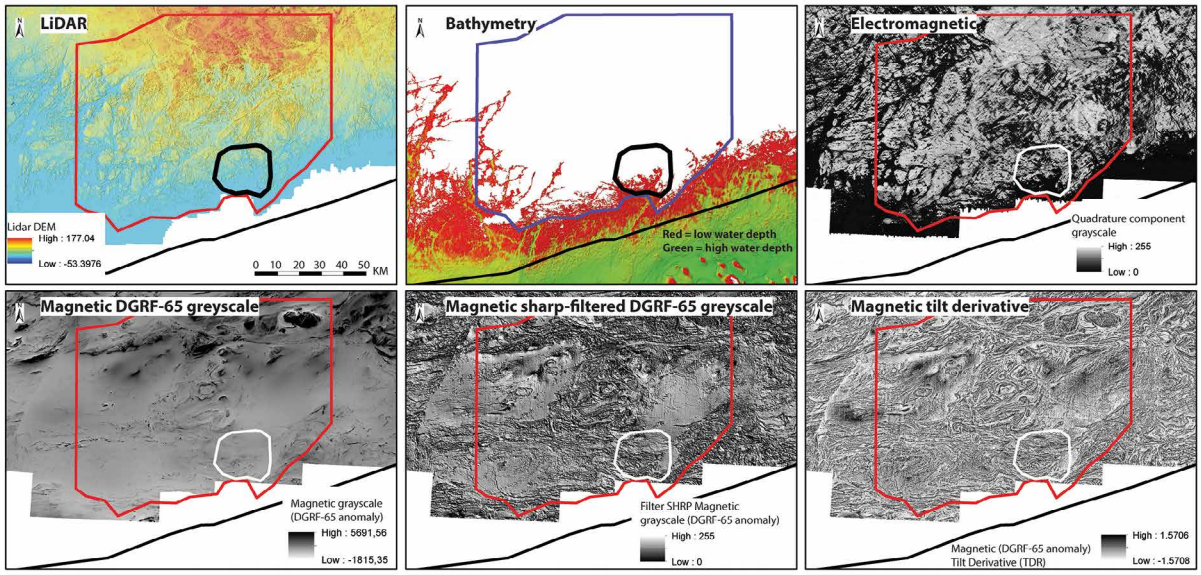

Figure 3. Source data for lineament mapping, visualised for the Hanko–Helsinki study area.

electromagnetic minima regarding both the 1:500k and 1:200k study areas (Table 2). Since brittle structures increase the porosity and permeability of crystalline rocks, they are typically associated with hydrothermal processes, which in turn increase or decrease the magnetic susceptibility of the bedrock and lead to positive or negative magnetic anomalies along brittle deformation zones. Also, the low temperature weathering of fractured rock decreases the magnetic susceptibility. Furthermore, the presence of sedimentary infill and the contained groundwater within the topographic depressions above brittle deformation zones lowers the magnetic field and increases the electrical conductivity. Thus, linear magnetic and electrical anomalies within geophysical datasets can be used in mapping of geophysical lineaments. The basis for geophysical lineament mapping is explained in more detail in Paananen (2013) and references within, and in Middleton et al. (2015). Since most of the aerogeophysical data were collected from an altitude of 30 m with a line spacing of 200 m, the resolution of the data is unsuitable for full-resolution mapping.

Lineaments were first mapped separately from topographic (including LiDAR and bathymetry), magnetic and electromagnetic data and later merged into one integrated lineament dataset for 1:500k and 1:200k resolutions. We used the topographic lineaments as a basis for the integration, since the resolution of the LiDAR DEM was highest and most recent of all the rasters and thereby considered most accurate. However, a significant number of lineaments were mapped only from the geophysical data. The integrated 1:500k dataset consists of 33% unmodified topographic lineaments, 17% lineaments based on both topographic and geophysical information and 50% geophysical lineaments. The integrated 1:200k dataset consists of 73% unmodified topographic lineaments, 14% lineaments based on both topographic and geophysical information and 13% purely geophysical lineaments. We used the integrated lineament dataset in our data analysis, except for the full-resolution data, which are only based on LiDAR mapping due to the limited resolution of the other datasets.

In the case where lineaments continue outside of the study areas, lineaments were digitised for their total observable length. For 1:500k and 1:200k mapping, the resolution of the datasets, allows for relatively uncensored lineament mapping of large

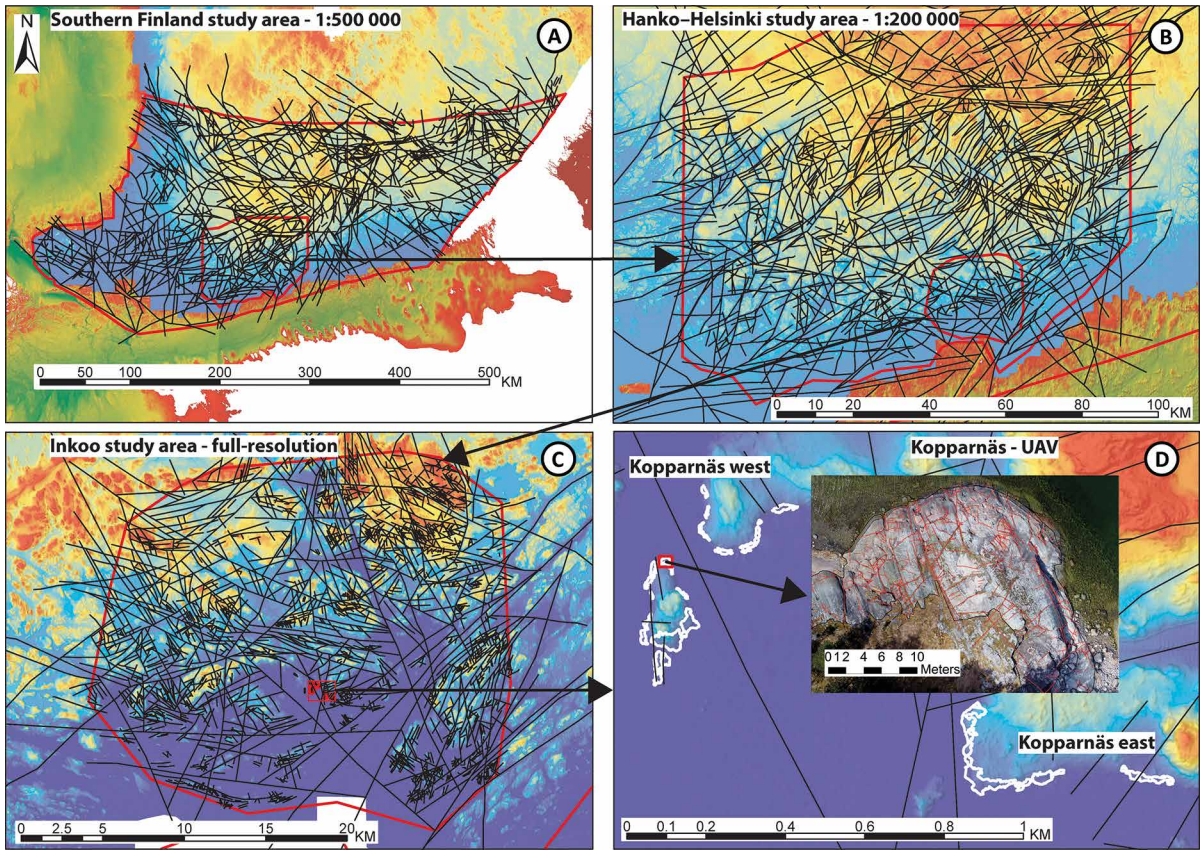

Figure 4. Visualisation of the different study areas, the mapped lineament datasets (a-c) and the UAV data (d). The study areas are outlined by red lines and the lineaments are displayed as black lines on top of LiDAR data. In a) and b), parts of the bathymetric data are also visible for offshore areas. d) The areas of mapped UAV data displayed as white polygons (categorized into western and eastern localities). The inset shows a zoom in to one of the imaged outcrops with digitised fracture traces in red.

features. However, since many of the full-resolution lineaments represent relatively small structures, they are more often censored (e.g. when continuing into areas covered by water). Due to the low resolution of the bathymetric data (115 m^2/pixel), the full-resolution lineaments, representing small and localised topographic depressions were not possible to capture. Therefore, the bathymetric data were only useful for the 1:500k and 1:200k resolutions. Consequently, full-resolution lineaments are regularly truncated by water (Fig. 4c).

We acknowledge that some of the mapped lineaments in our database coincide with glacial features. However, since many glacial landforms, such as subglacial meltwater routes, eskers and glacial lineaments, are known to be controlled by underlying brittle structures (Henderson 2011), we chose not to discard these features from our lineament dataset. To compare the impact of glacial erosion on our lineament datasets, we used available generalized ice-flow directions related to the known patterns of the Late Weichselian ice sheet (Punkari 1997; Boulton et al. 2001; Putkinen et al. 2017) for the southern Finland and Hanko–Helsinki study areas, together with the regional point observations of glacial striations maintained in the HAKKU service by the Geological Survey of Finland (https://hakku.gtk.fi/en/). For the Inkoo study area, glacial striations are based on the data available in the HAKKU service.

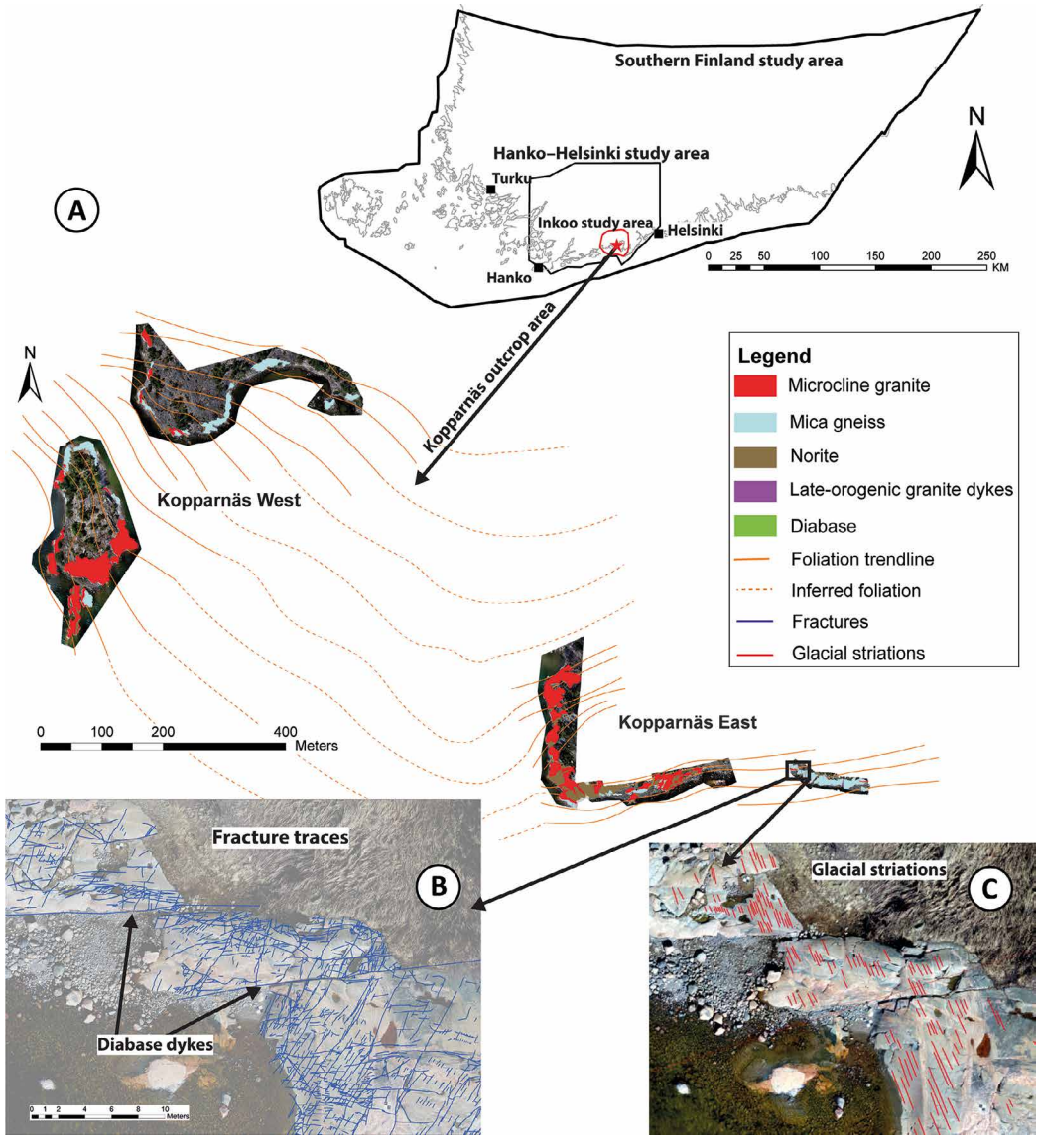

Figure 5. a) Location, lithology and foliation of the Kopparnäs outcrop area, b) fracture traces mapped from UAV data (diabase dykes indicated by arrows) and c) glacial striations mapped from UAV data. The areas with a lithology symbol overlay in 5a, represent the clean UAV-mapped outcrops.

4.2. Tracing of outcrop features from the UAV data

We used UAV imaging techniques (Table 2) for high-resolution photogrammetric documentation (Bemis et al. 2014; James et al. 2019) of an outcrop area ~1 km^2 in size, along the coastline of the Kopparnäs peninsula (Fig. 4d; Fig. 5a). The separate outcrops are polished and range in size from tens to hundreds of metres in the direction of the shorelines. Inland, the polished parts of the outcrops usually only extend a couple of tens of metres before becoming covered by moss and lichen, restricting the identification of geological features (Fig. 5b). Based on the location of the outcrops, the Kopparnäs outcrop area was divided into eastern

Table 2. Summary of data sources used for generating the lineaments and fracture traces

Data/method	**Type**	**Source**	**Resolution**	**Represented feature**	**Visualization**	**Study area(s)/dataset(s) (See Table 1)**
LiDAR*	Topography	Geological Survey of Finland	2 m/pixel	Topographic linear low: brittle deformation zone, potentially glacial feature	MDOW hillshade, slope****	Southern Finland/1:500k, Hanko–Helsinki/1:200k, Inkoo/full-resolution
Bathymetry	Topography	EMODnet Bathymetry Consortium	115 m/ pixel	Topographic linear low: brittle deformation zone, potentially glacial feature	Coloured elevation	Southern Finland/1:500k, Hanko–Helsinki/1:200k
Aerogeophysics**	Electromagnetic (EM) & magnetic (Mag)	Geological Survey of Finland	200 m/pixel	EM low: sediment + water–filled topographic depression associated with a fault. Mag. low: altered fault characterized by e.g. decomposed magnetite. Mag. high: altered fault represented by e.g. magnetite precipitation **	EM = 3kHz quadrature component greyscale. Mag = DGRF-65 greyscale, sharp-filtered total field DGRF-65 greyscale and tilt derivative *****	Southern Finland/1:500k, Hanko–Helsinki/1:200 k
UAV photogrammetry***	RGB images	This study	0.82 cm/pixel	Outcrop fractures	RGB orthomosaic images	Kopparnäs/UAV
Detailed UAV photogrammetry	RGB images	This study	0.11 cm/pixel	Outcrop fractures	RGB orthomosaic images	Kopparnäs/detailed UAV
Field mapping	Field observations	This study	na	Outcrop features	na	Kopparnäs

* Abdullah et al. 2013; Soliman and Han, 2019, ** Paananen et al. 2013 (and references within), *** Bemis et al. 2014; James et al. 2019; Ovaskainen et al. 2022, ****Palmu et al. 2015, *****Verduzco et al. 2004

and western parts (Fig. 4d). For the UAV missions and photogrammetric processing of georeferenced orthomosaic images, we followed the same workflow as previously utilised by Ovaskainen et al. (2022), but with differences in the flight altitude. Nadir imaging was performed from a 30 m altitude, resulting in a ground sampling distance (GSD) of 0.82 centimetres/pixel. Some smaller areas were reimaged from an altitude of 4 m with a 0.11 centimetre/pixel GSD. The UAV data from 30 m altitude are referred to as "UAV data" and the UAV data from 4 m altitude as "detailed UAV data".

We utilised the georeferenced two-dimensional orthomosaic images for tracing the main lithological units (Fig. 5a), the fracture network (Fig. 5b), and glacial striations (Fig. 5c) in ArcGIS (© ESRI). For digitizing UAV data, we were restricted to the polished parts of the outcrops where these features could be distinguished and traced from the images. A study area was therefore defined for the polished part of the outcrops, and only fractures crossing this area were digitised. If possible, however, fracture traces continuing outside of the study area were digitised for their observable length. However, in many cases, vegetation and water causes censoring of some of the longest outcrop fractures.

In addition to the UAV surveys, on-site field reconnaissance of the remotely mapped features was performed, including field measurements of foliation. This field work included general validation of the accuracy of the UAV datasets (fractures and glacial striations) with regards to orientation, topology, length and their geological significance. Based on the field validation, remotely mapped traces for glacial striations were found to be representative and well discernible from fracture traces. The detail of short individual fracture traces was, however, found to be limited by the resolution of the UAV images. For example, individual sub-metre fractures, fracture segments or fracture branches were not always consistently mapped.

5. Scalability of the multiscale datasets: methods and results

5.1. Topology

Topology describes the relationship between fractures and the connectivity of a fracture network (Sanderson & Nixon 2015, 2018; Thiele et al. 2016). To enable topological analysis of the lineament and UAV data (two-dimensional polylines), the polylines that abut to other polylines were digitised using the snapping function of ArcGIS (© ESRI) according to the workflow described in Nyberg et al. (2018). For topological analysis we use a newly developed Python library, *fractopo* (Ovaskainen et al. 2022), which is inspired by and follows similar principles to *NetworkGT* (Nyberg et al. 2018). Using the library, we determined the topological branches and nodes for each scale dataset of either lineaments or fracture traces. Furthermore, we calculated and plotted the relative counts of node (X, Y and I) and branch types (C–C, C–I and I–I) according to the methodology described in Sanderson & Nixon (2015). We used the connections per branch parameter $C_B = (3N_Y + 4N_X)/N_B$ to calculate a measure of connectivity of the fracture network (Sanderson & Nixon 2015).

The topological results in Fig. 6 demonstrate that lineaments within 1:500k and 1:200k resolutions form a highly connected network with more X-nodes compared to the full-resolution lineaments and the UAV data, which are dominated by I- and Y-nodes. The connections per branch (C_B) values of over 1.8 for 1:500 k and 1:200k lineaments, represent networks of interconnected large features, while especially the UAV data (average C_B value of 1.35) contain a relatively low degree of connected nodes.

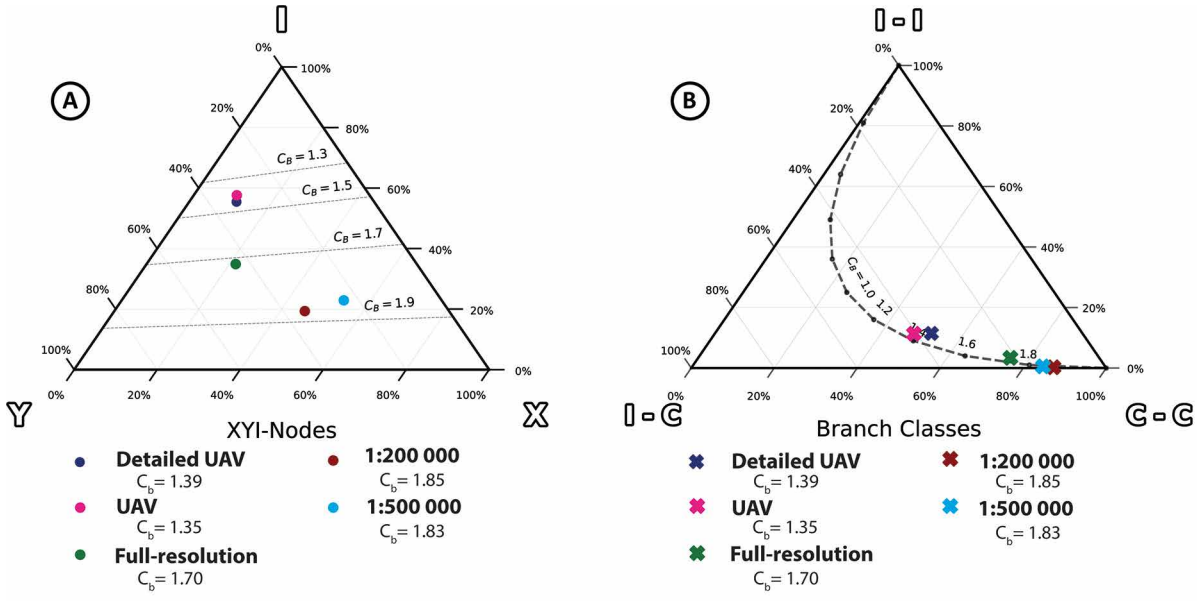

Figure 6. Overall topological properties for the different datasets, visualised as both a) node types and b) branch classes. C_B stands for the connections per branch parameter.

5.2. Orientation

For orientation analysis, we used the information from the sublinear two-dimensional traces based on the orientation trend between the first and last point of the trace. We visualised these trend data with length-weighted equal-area rose plots according to the workflow recommended by Sanderson & Peacock (2020). We analysed the orientation trends of all lineament datasets and the UAV data from Kopparnäs (Fig. 4d). In addition, we compared the rose plots of lineaments with the trends of ductile foliation and glacial flow. For all three lineament scales, the lineament orientations were compared with foliation observation data maintained by the Geological Survey of Finland (https://hakku.gtk.fi/en/). For the UAV data, we compared the fracture trend data with our outcrop foliation measurements.

Orientation data from the area of southern Finland are quite scattered (Fig. 7a) and the different lineament datasets show some variation in the orientation of the main lineament sets (Fig. 7 a–c; Table 3). Based on a comparison between the orientation of the different lineament datasets within the Inkoo study area (Fig. 7c–e), all three lineament scales capture similar main lineament sets, consisting of NE–SW, NNW–SSE and ESE–WNW trending ones. The NE–SW to NNE–SSW trend maxima, observed within all lineament datasets, correlates with the trend of glacial flow. A consistency between lineament maxima and foliation is only observed for the ENE–WSW set of the Hanko–Helsinki study area and the ESE–WSW set of the Inkoo study area (Fig. 7; Table 3).

Due to the lithological heterogeneity, UAV fracture orientation data from Kopparnäs are quite scattered (weak maxima around 40 and 90 degrees are nevertheless present), while the data for glacial striation measurements cluster at 340° (Fig. 5c; Fig. 7f). This represents a slight local deviation from the average 330° regional FIS ice-flow direction (Fig. 7a–c). The foliation in the western region of the surveyed area is dominated by a NW–SE trend, albeit with some scatter in the data, that contrasts with the strong E–W trend to the east of the surveyed area. Therefore, fracture orientations are analysed separately within the western and eastern parts of the area. This analysis

Table 3. Main orientation trends of the different datasets.

	Main orientation sets			Foliation	Glacial flow
Dataset	**1**	**2**	**3**		
1:500 k	Scattered			Scattered	NNW–SSE
1:200 k	ENE–WSW	NNW–SSE		ENE–WSW	NNW–SSE
Full-resolution	NE–SW	NNW–SSE	ESE–WNW	ESE–WNW	NNW–SSE
UAV	NE–SW	E–W		Scattered	NNW–SSE
UAV-West	NE–SW	NW–SE		NW–SE	NNW–SSE
UAV-East	NE–SW	E–W		E–W	NNW–SSE

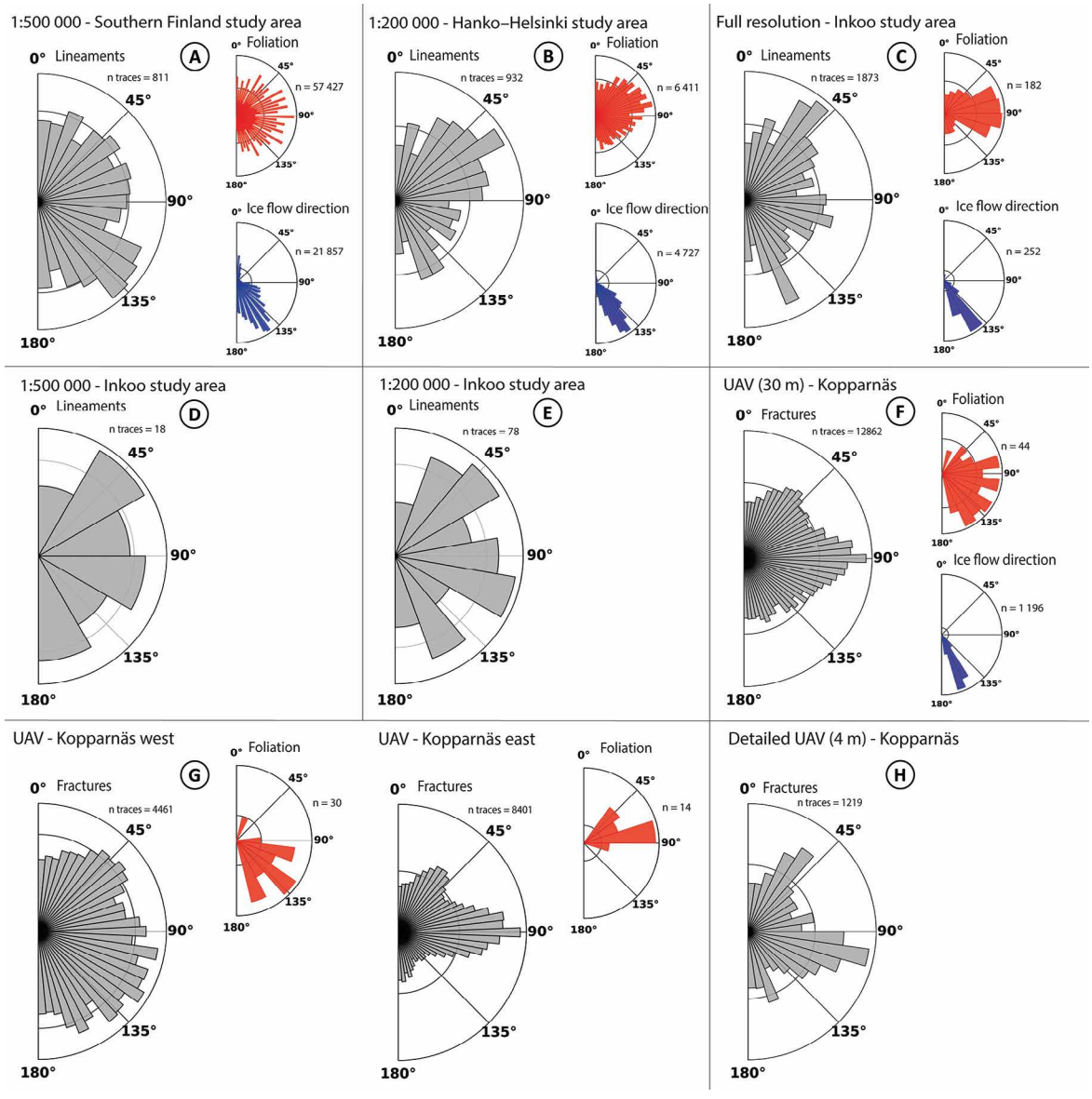

Figure 7. Length-weighted rosette plots of lineament trends for the different study areas (grey plot). For comparison, foliation (red plot) and the FIS ice-flow directions (blue plot) are included. a) 1:500k resolution, southern Finland study area, b) 1:200k resolution, Hanko–Helsinki study area, c) full-resolution, Inkoo study area, d) 1:500k resolution, Inkoo study area, e) 1:200k resolution, Inkoo study area, f) UAV data, Kopparnäs area, g) comparison between the eastern and western Kopparnäs areas, h) detailed UAV data.

revealed a NE–SW trending fracture set for both areas, while another prevailing set correlated with the trend of the foliation, being on average NW–SE trending in the west and distinctly E-W trending in the east (Fig. 7g). The higher level of scattering in the western area, of both foliation and fracture orientation, can be explained by open folding of the migmatitic foliation (Fig 5a). The detailed UAV data display similar fracture trends to the UAV data (Fig. 7h).

5.3. Length distribution

The lengths of the digitized fracture and lineament traces can be statistically analysed to reveal characteristics of their length distribution. We used the total length of the traces, which thus included continuations of traces outside of the study areas. Our UAV datasets included digitized fractures from the centimetre scale up to tens of metres, while the lineaments range between tens of metres and 300 kilometres long. For each scale of observation individually, the trace length data were analysed using a Python library, *powerlaw* (Alstott et al. 2014), to fit the power law, lognormal and exponential distributions to the length data. However, due to well-known sampling truncation issues related to the digitization process of both fractures and lineaments the lowest trace lengths within each scale are not sampled correctly. Due to this, a cut-off must be applied to the length distribution data to fit a power-law (Bonnet et al. 2001). We determined the cut-off automatically using the *powerlaw*-library. The cut-off represents the minimum length to which data follows a potential power law distribution. The *powerlaw*-library determined the minimum length by calculating power law fits to the probability density distribution of the lengths with all possible cut-offs and by selecting the one that resulted in the lowest Kolmogorov-Smirnov distance (Alstott et al. 2014). The fitting uses maximum likelihood estimators and follows the process defined by Clauset et al. (2009). All other distributions were fitted to the same, cut-off truncated, data to accurately compare the fits using log-likelihood ratios (Clauset et al. 2009; Alstott et al. 2014). Following Bonnet et al. (2001) and Clauset et al. (2009), we defined the power law length distribution ($n(l)$) as $n(l) = A \times l^{\alpha}$, where A is a constant, l is the fracture trace length and α is the power law exponent. We compared the fitted distributions with each other to determine the log-likelihood ratio, R, and the significance value of the ratio, p, for each comparison pair (power law vs. lognormal, power law vs. exponential, etc.). R can be negative or positive, depending on which fit is more likely in a comparison, and p signifies the reliance of R. For values of p above 0.1, we interpret the ratio as nonsignificant, as recommended by Clauset et al. (2009). In combination, these values were used to resolve the best distribution fit for each dataset (Table 4).

To analyse the scalability of multiscale length data, the length data from different scales must be normalised (Bonnet et al. 2001). A typically used normalisation method uses the area of the study area from which the traces are digitized, to divide the (complementary) cumulative distribution of the traces (e.g. Odling et al. 1997; Odling et al. 1999; Bertrand et al. 2015; Bossenec et al. 2021; Chabani et al. 2021). An alternative is using the fractal dimensions along with the areas of each scale trace datasets, to normalise the probability density distribution (e.g. Davy et al. 1990; Bonnet et al. 2001; Bour et al. 2002; Davy et al. 2006). We used the former, simpler and readily available method of area-normalisation of the cumulative distribution, to enable comparisons to the numerous studies that use the same method and to avoid the uncertainties related to defining the fractal dimensions for our irregularly shaped and discontinuous study areas. We first normalised the length data from different scales with their area and then used the single scale cut-offs determined earlier from individual scale datasets by *powerlaw* to truncate the data. The *powerlaw*-library does not provide utilities for fitting a power law to multiscale data, we consequently used a simple first-degree polynomial least squares fit algorithm to determine a power law trend that fitted the multiscale length data as implemented in

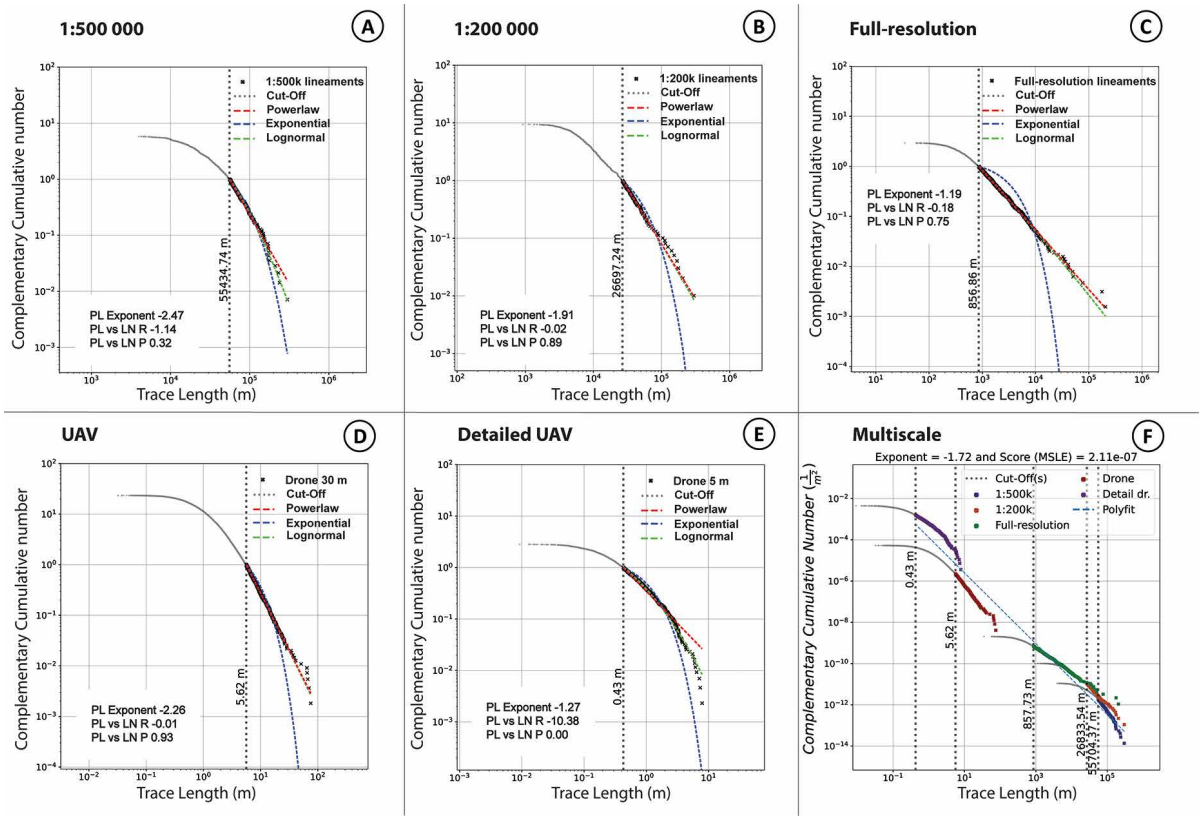

Figure 8. Exponential, lognormal and power law length distributions for the five different scales and multiscale. Plots a–e present the truncated data after the assignment of a lower cut-off for each scale, while plot 4f displays each truncated scale dataset, normalised for area, along with a common multiscale power law exponent fit. Parameters of the power law vs. log normal length distribution analysis are included for each dataset. PL = power law, LN = lognormal, R = likelihood ratio (positive when x is more likely in x vs. y and negative when y is more likely) and P = the significance of R (the smaller the P value, the more statistically significant the result of R is).

fractopo (Ovaskainen et al. 2022). The polynomial was fitted to the logarithm of the lengths and the logarithm of the complementary cumulative numbers. The first coefficient of this fit is the power law exponent.

Applying the automatic cut-off for trace length data resulted in the omission of between 65.82% and 95.73% of the data within each dataset (Table 4). The plots a–e in Figure 8 contain the truncated length data along with the three length distribution fits, while truncated data from all scales are displayed in Figure 8f. For all datasets, the exponential distribution was the least fitting according to the values of R in comparison to both power law and lognormal distributions (Fig. 8). The R-values in lognormal versus power law comparisons favoured lognormal for all datasets, although with high p-values for the 1:200k resolution (0.89), full-resolution (0.75) and UAV data (0.93). The high p-value indicates low significance of the respective R-values, and consequently decreases the certainty that lognormal is strictly a better fit. The p-value for 1:500k resolution is somewhat lower (0.32), but not low enough (<0.10) to completely rule out the power law distribution as a good fit in comparison to lognormal (Clauset et al. 2009). The detailed UAV data were the only dataset for which the results strongly supported lognormal over all other distributions (Table 4).

The power law exponent represents the relative number of longer versus shorter lineaments, and

Table 4. Main parameters of the length distribution analysis. PL = power law, LN = lognormal, EX = exponential, R = log-likelihood ratio and P = the significance of R. The smaller the P-value, the more statistically significant the result of R is.

Name	PL exponent	PL sigma	PL cut-off (m)	PL cut-off %	LN mu	LN sigma	EX lambda	PL vs LN R	PL vs LN P	PL vs EX R	PL vs EX P	LN vs EX R	LN vs EX P
1:500k	-2.47	0.21	55 435	82.86	9.38	0.96	2.94	-0.99	0.32	0.50	0.61	1.21	0.23
1:200k	-1.92	0.19	26 697	89.48	-13.72	3.61	3.75	-0.14	0.89	2.27	0.02	2.32	0.02
Full-resolution	-1.19	0.05	857	65.82	-24.53	5.26	0.00	-0.32	0.75	4.04	5.42	4.06	4.89
UAV	-2.26	0.10	5.62	95.73	-63.175	5.40	0.23	-0.09	0.93	3.65	0.00	3.68	0.00
Detailed UAV	-1.25	0.06	0.43	64.64	-1.64	1.31	1.24	-2.92	0.00	1.81	0.07	3.64	0.00

a lower exponent denotes that the truncated data have a relatively minor number of long features compared to shorter ones. The power law exponents of our datasets vary between -1.19 and -2.47 (Table 4). The truncated 1:500k lineament data have the lowest power law exponent of -2.47, revealing that this dataset contains the lowest relative number of long features compared to shorter ones. The truncated full-resolution lineament dataset has the highest power law exponent of -1.19 and is thereby the dataset with the relatively highest number of long features compared to shorter ones. The high variation in exponent values between datasets would suggest that they do not follow a common length distribution. However, the 1:200k and the UAV datasets are relatively close, with exponents of -1.92 and -2.26, respectively. The difference in the goodness of fit between lognormal and power law distributions, tested with the log-likelihood ratio R, is smallest at these two scales, while larger values for *R* are observed when comparing lognormal to power law for 1:500k resolution, full-resolution and detailed UAV data (Table 4).

5.4. Appearance of full-resolution lineament length classes

To analyse the possible localisation of fault zones at lithological contacts, we investigated the correlation of length with the distance from lineaments to major lithological contacts in the bedrock. We extracted the lineament data from the full-resolution lineament dataset, consisting of lineaments varying between 35 m and 205 km in length, into length classes of <500 m, 500–1 000 m, 1 000–5 000 m, 5 000–10 000 m, 10 000–50 000 m and > 50 000 m. Since shorter lineaments are significantly more abundant than longer ones, the three shortest classes contain a considerably higher amount of data compared to the three longest ones.

The lineament distances from the rock type boundaries (Geological Map of Finland – Bedrock 1:1 000 000 © Geological Survey of Finland 2016) were studied by transforming the lineaments into points using 50-m intervals and calculating the distance from the nearest rock type boundary. The distances from the nearest rock type boundary within the lineament length classes were visualised as boxplots. To investigate the level of surface exposure of the bedrock for different lineament length classes, the Quaternary deposit type (Superficial deposits 1:20 000 © Geological Survey of Finland 2015) at the location of the lineaments was examined by cutting the lineaments at the boundaries of (> 1 m thick) Quaternary deposits and calculating the percentage of the total length of lineaments in the soil types. The percentages within the lineament length classes were visualised as boxplots.

Analysis of the potential control of underlying heterogeneity of the bedrock (Fig. 9) suggested a correlation between the spatial distribution of lithological contacts and the two longest lineament length classes, >10 km in length. However, due to the small number of lineaments in the two largest length classes statistical uncertainty remains.

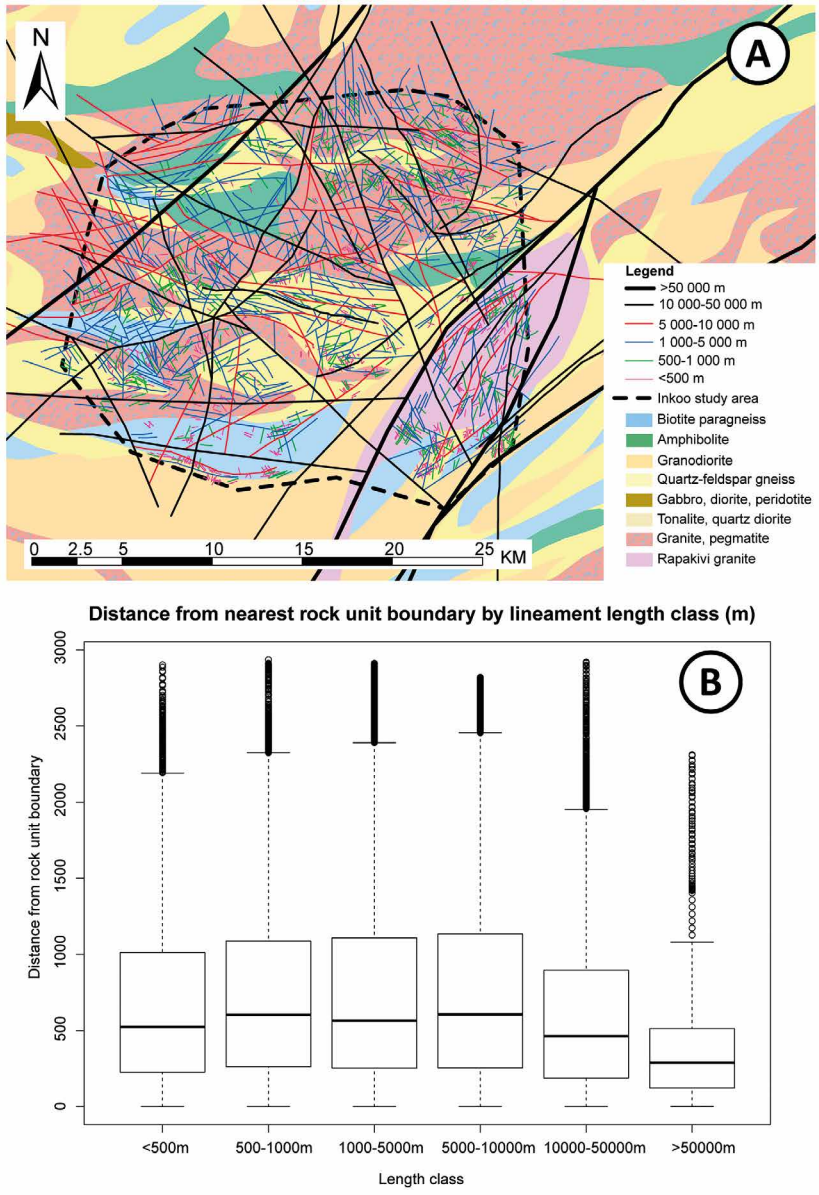

Figure 9. a) Full-resolution lineaments (Inkoo study area) visualised as different length classes on a generalised lithological map (Geological Map of Finland – Bedrock 1:1 000 000 © Geological Survey of Finland 2016). b) Boxplot visualizing the distance from the nearest rock unit boundary by lineament length class.

Analysis of the potential correlation between lineament length and bedrock erosion (Fig. 10a) and of the occurrence of different sediment types or water along the lineaments (Fig. 10b) indicated a negative correlation between areas where the bedrock is at a depth <1 m and lineament length. The shorter length classes typically occur in well-exposed areas and the longer ones are more often hidden beneath a >1-m-thick sedimentary cover and water. The results also revealed that lineament length correlates positively with the occurrence of clay, gyttja, peat and water. Other surficial deposits did not show a clear correlation with lineament length class. Based on our field mappings at Kopparnäs, most remotely mapped UAV fracture traces represent tensional joints, while very few fault structures were identified from the outcrops, with one of the few exceptions being a possible fault damage zone observed as an elevated fracture intensity at the northern rim of Kopparnäs East. In this location, a full-resolution lineament has also been mapped (Fig. 4d).

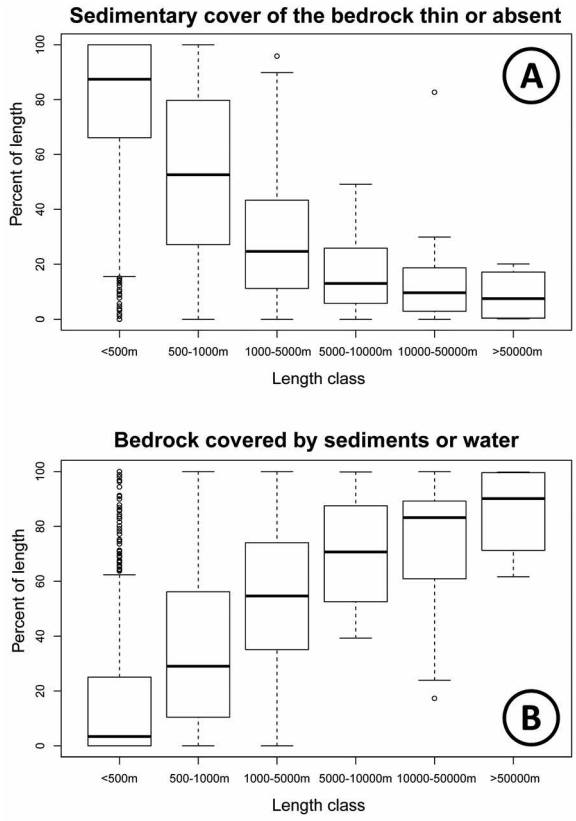

Figure 10. Lineament length classes analysed for the depth of bedrock <1 m (a) and for the occurrence of clay, gyttja, peat or water along their strike (b). Percentage of length = percentage of the total lineament length in the soil types.

6. Discussion

6.1. Assumptions for lineaments

As observed in on-site field reconnaissance of the Kopparnäs outcrops, our UAV-based fracture datasets (Table 2) mainly represent joints. Conversely, we assume the lineaments, mapped in lower resolution, to mainly represent fault structures. We base this assumption on results from the site for spent nuclear fuel in Olkiluoto (south-western Finland), where lineaments have been found to regularly represent brittle fault zones (Aaltonen et al. 2016). In addition, observations by Nordbäck (2014) indicated that in the vicinity of Olkiluoto: 1) individual joints seldom exceed 50 m in length; 2) shear fractures are regularly over >50 m in length, but seldom >100 m long; 3) >200-m-long brittle structures are typically fault zones with a macroscopically visible core and damage zones. Assuming a similar pattern for the Inkoo study area, none or very few of the full-resolution lineaments should represent joints, but different types of fault structures (shear fractures and fault zones) instead. Accordingly, 1:500k and 1:200k lineaments, restricted to >1-km-long structures, should be solely representative of fault zones. Nevertheless, as our lineaments are unverified structures, we refer to these datasets only as lineament data.

6.2. Data quality assessment and uncertainties

Since different resolution datasets can be affected by different levels or types of censoring and biases (Bond et al. 2007; Scheiber et al. 2015; Andrews et al. 2019), it is important to evaluate the related uncertainties and limitations separately for each scale.

The accuracy with which lineaments can be identified is affected by the thickness of the sedimentary cover, the extent of censored regions, the resolution of source datasets, and the scale of observation. Larger lineaments (inferred fault zones) promote stronger erosion of their immediate surroundings compared to shorter ones (Fig. 10). This enhanced erosion is related to the development of wider damage zones (Cowie & Scholz 1992; Schlische et al. 1996), which results in wider topographically censored and sedimentary filled depressions in the bedrock, where observing details of lineaments and topological relationships between lineaments may become challenging or even impossible. Such sedimentary censoring could also potentially lead to multiple smaller structures being mapped as one long lineament. Furthermore, since the resolution of bathymetric and geophysical data is not adequate for mapping at the full-resolution, this dataset is also highly affected by censoring and the truncation of shorter lineaments within

sedimentary and water-covered areas, adding to the challenges in interpreting topological relationships between lineaments.

The rough scale of observation within the 1:500k resolution adds to the uncertainties within this dataset. For example, separate lineaments that are located in close proximity, may appear as one lineament at this scale of observation. This issue is mostly avoided within the 1:200k resolution, which still allows for relatively accurate lineament mapping of large areas within a reasonable time. Nevertheless, for areas where the topography is smoothened by Quaternary sediments, lineaments representing individual fault zones or segments thereof are not necessarily recognized, even when zooming into the full resolution of the LiDAR data (Fig. 10). Therefore, the possibility to integrate the topographic and geophysical data at 1:500k and 1:200k resolutions provides additional information, especially in areas of sedimentary cover. Although the full-resolution has the potential to capture a broader scale of lineaments compared to the 1:200k resolution, smaller brittle features have smaller damage zones, which are less susceptible to enhanced erosion. Consequently, based on our assessment, small structures do not cause topographic anomalies that remain visible beneath even relatively thin sedimentary layers (Fig. 10), and mapping of <1-km-long topographic lineaments is therefore highly reliant on the availability of well-exposed bedrock areas.

Although the fractures observed and mapped directly from the outcrop UAV images are less affected by subjectivity compared to the mapped lineaments (Scheiber et al. 2015), we acknowledge that a certain level of subjectivity is still associated with the distinction between, for instance, one long continuous fracture trace vs. a fracture consisting of several shorter interconnected segments (Andrews et al. 2019). This problem is linked to the limitations in resolution, which makes it difficult to accurately detect all the smallest details of fractures. This can be pointed out by comparing the fracture length power law cut-offs between the 30-m-altitude UAV data and the 4-m-altitude detailed UAV data, where the cut-off is 5.62 m in the former and 0.43 m in the latter (Table 4). Furthermore, since outcrops represent the more preserved parts of the bedrock (Scott & Wohl 2019) and are limited in size, large brittle structures are typically not observed in the outcrops. This limitation also causes censoring of some of the longer fractures, which cannot be mapped for their actual total lengths (Zeeb et al. 2013). The effect of censoring is negligible for the detailed UAV data, which were only collected from the central parts of the outcrops.

6.3. Topology

The censoring effects described in chapter 6.2 significantly lower the reliability of the topological analysis results, especially with regards to the full-resolution and 1:500k datasets. Since the full-resolution lineaments within the Inkoo study area are regularly truncated by water and sediments, this dataset probably includes an erroneously high number of disconnected branches. Consequently, the C_B value of 1.7 (Fig. 6) is also probably an underestimation of the actual connectivity within this scale. Considering that the area of southern Finland includes areas with relatively thick sedimentary cover, and since enhanced erosion around the largest lineament features is observed to cause further censoring, the C_B value of 1.83 for the 1:500k dataset (Fig. 6) is possibly also an incorrectly low estimate. Although we regard the 1:200k dataset as the most reliably sampled lineament dataset, we acknowledge that there still is a high level of uncertainty associated with the interpretations of topological relationships at this resolution. The C_B value of 1.85 for the 1:200k dataset (Fig. 6) is almost equivalent to the value of 1.83 for the 1:500k dataset. However, the 1:200k data contains a higher relative number of Y-nodes than the 1:500k data, which indicates a higher percolation threshold (Sanderson & Nixon 2018). The rough scale of observation at the 1:500k resolution, however, could cause two closely spaced Y-nodes to be misinterpreted as an X-node.

Topological analysis of the detailed UAV data and UAV data revealed almost identical results of 1.39 and 1.35, respectively, for the C_B parameter and the relationship between node types (Fig. 6). This highlights the possible effect of the scale of observation, where not all details, such as interconnected fractures or branched features, are as accurately observed in the UAV data as in the higher resolution detailed UAV dataset. The clearly higher C_B values for the lineament sets are logical due to the higher ability of fault structures to intersect each other compared to joints, with the latter more often abutting pre-existing joints (Peacock et al. 2017, 2018).

The scale of observation has implications for topological lineament results (Bertrand et al. 2015; Ovaskainen 2020). At a higher resolution, structures are in fact composed of many smaller structures (Tchalenko 1970; Bonnet et al. 2001) than when observed at a lower resolution. Therefore, in addition to the uncertainties of our lineament datasets, the scale of observation is also important to keep in mind when comparing topological data between scales.

6.4. Evaluation of orientation trend data

Joints and fault structures are controlled by variations in rheology and the mechanical strength of different lithologies (Miller & Paterson 2001), which may cause local changes in the intensity, orientation and localisation of brittle structures. In addition to mechanical anisotropies, spatial variation can also be caused by brittle compartmentalisation of the bedrock and resulting stress perturbations (Maerten et al. 2002; Gudmundsson et al. 2010). When investigating the whole of southern Finland within the 1:500k resolution (Fig. 7a), a large scatter in lineament and foliation orientation data is observed, apparently related to crustal heterogeneities such as major lithological (Fig. 1) and ductile domains. A more distinct pattern and similarity between the orientation trend data is observed when comparing only the 1:200k resolution and full-resolution datasets (Fig. 7b–c), sampled within geologically similar areas. Accordingly, when analysing the three lineament datasets only for the Inkoo study area, all three datasets capture similar main trends for lineaments (Fig. 7c–e). Nevertheless, with an increasing amount of data towards detailed scales, orientation sets become better defined, with the 1:200k resolution already corresponding quite well with the main sets of the full-resolution data. Thus, our results indicate that the orientation of lineaments is independent of scale but affected by variations in rheology.

The 1:200k dataset shows the association of the prevailing NE–SW trending lineament set and the main orientation of foliation, and the full-resolution datasets between E–W trending lineaments and foliation (Fig. 7). However, since the anisotropies of the bedrock in southern Finland, such as ductile structures and lithological contacts are known to have a strong control on the localisation of brittle structures (Elminen et al. 2008; Pajunen et al. 2008; Skyttä & Torvela 2018), we regard lineaments parallel to foliation as also being representative of brittle structures. Major ductile shear zones within the 1:200k area, including the NE–SW trending Kisko and Porkkala–Mäntsälä shear zones, were also reactivated within the brittle domain (Ploegsma & Westra 1990; Heeremans & Wijbrans 1999; Väisänen & Skyttä 2007; Elminen et al. 2008). Based on the mapped lineaments, other NE–SW trending structures probably occur in between the previously studied ones (Fig. 2 and Fig. 4b). Elminen et al. (2008) described E–W trending fault structures from the Helsinki area as strike-slip faults, localized by E–W trending mylonitic precursors. Presumably, the E–W trending lineament set within the Inkoo study area represents similar ductile shear structures that were reactivated within the brittle regime. The localizing control of ductile precursors on later formed joints is also visible from our UAV data (Fig. 7f-g), which reveal that one main fracture set is always developed parallel to the trend of foliation, despite a switch in foliation orientation in

different parts of Kopparnäs. The lack of an NNW–SSE trending set within the UAV data (Fig. 7), observed within the lineament datasets, indicates that the scalability of orientation is only valid for joints and lineaments separately.

Since the trend of the NNW–SSE lineament set is parallel to the trend of glacial striations (Fig. 7), the potential impact of glacial erosion (Glasser et al. 2020) causes uncertainty in the degree and accuracy with which these lineaments represent brittle structures. Currently, it cannot be verified whether such lineaments are possibly overrepresented within our datasets or if major brittle structures could perhaps have partly steered the glacial flow (Krabbendam & Bradwell 2014). However, due to the confirmed existence of a NNW–SSE-trending group of brittle faults for the Helsinki region (Elminen et al. 2008), we assume our NNW–SSE trending lineament set to be representative of similar brittle structures.

6.5. Length distribution

The 1:500k lineament dataset, with a power law exponent of -2.47 (Fig. 8a; Table 4), represents the dataset with the lowest ratio of long lineaments compared to short ones. The reason for this small exponent compared to our other datasets remains uncertain, but it could be caused by the local control of pre-existing weaknesses in the bedrock, such as lithological heterogeneities and/or ductile precursors. In Figure 9, we observe that the spatial localisation of lineaments greater than 10 km in length is guided by major lithological contacts and ductile shear structures. While serving as mechanical weaknesses within the bedrock, it is possible that such reactivated anisotropies have segmented the brittle framework and restricted the development of additional brittle structures (Munier & Talbot 1993) over certain lengths. Furthermore, a limited thickness of the brittle crust is also known to limit the scale at which power law distributions can occur (Cowie et al. 1995; Odling 1997; Cowie 1998; Bonnet et al. 2001). Thus, it is possible that the 1:500k dataset (power law cut-off at 55 km) crosses the upper limit for another length-distribution, possibly occurring within the smaller scale structures. However, the biases caused by scale dependent censoring and other methodological issues, as discussed in chapter 6.2, are too large to draw conclusions based on this dataset alone.

The 1:200k lineament dataset with a power law exponent of -1.92 (Fig. 8b; Table 4) closely corresponds with the results reported by Ovaskainen (2020), from within the Wiborg rapakivi batholite. Although the 1:200k resolution was found to be best suited for capturing the details of lineaments, the <27 km cut-off still indicates that censoring of shorter lineaments remains an issue within this scale. The full-resolution power law exponent of -1.19 (Fig. 8c; Table 4) is the highest exponent in comparison to our other datasets. An explanation for this high exponent could be the partial masking of the Inkoo study area by sediments and water, which has resulted in a falsely low number of identified short lineaments compared to longer ones. In addition, most of the shortest full-resolution lineaments are also truncated due to this censoring.

The length distribution analysis of the UAV data and detailed UAV data reveals that the UAV data display a good fit to a power law length distribution with an exponent of -2.26, while the detailed UAV data only fit a lognormal distribution (Fig. 8d–8e; Table 4). By studying the length distribution data in Figure 8e for the detailed UAV data, a clear deviation from the fitted power law distribution is observable for fracture traces above 2 m in length. This apparent difference between fracture traces more than a couple of metres long and shorter ones is in line with the "universal fracture model" (UFM) described by Davy et al. (2010). According to this, fractures may either grow in a dilute regime, where fractures can grow more freely, or in a dense regime, where fracture growth has become controlled by mechanical interactions between discontinuities (Segall & Pollard 1983) and the abutment of shorter fractures to longer pre-existing ones (Peacock et al. 2018). According to the model by Davy et al. (2010), only the dense regime is expected to follow

a power law length distribution, while the smaller-scale fracture population (dilute regime) represents younger and less developed fracturing, which in our case follows a lognormal length distribution.

When comparing the different datasets in the multiscale plot in Figure 8f, the datasets roughly align around a common power law exponent of -1.72, which is not, however, a good fit with any of the individual datasets. Our method of fitting a first-degree polynomial fit to the logarithm of the multiscale length data could be improved, for example, by using the probability density function in place of the complementary cumulative number and by normalising by the fractal dimension and area rather than only by the area (Davy et al. 1990; Bonnet et al. 2001; Bour et al. 2002; Davy et al. 2006). As such, our multiscale analysis is a first-pass analysis of the data, and in later studies a more critical approach to choosing study areas and the methods should be applied to reduce the uncertainties present in our multiscale length analysis. Nevertheless, for the areas and resolutions we have studied, the 1:200k lineament data appear to offer a good estimate of the scalability of lineaments that are tens to a couple of hundred kilometres long, while the UAV outcrop datasets are suitable for the detailed characterisation of joint networks.

To better define the exponents and the size of the systems in which power law length distributions remain valid, future studies would need to be targeted to larger outcrop areas. Ideally, such areas should also be isotropic and include continuous well-exposed areas suitable for uncensored full-resolution lineament mapping. In the case of larger outcrop areas, the use of circular sample areas could also be beneficial to normalise the effect of possibly censored and truncated features (Mauldon 1998; Mauldon et al. 2001; Zeeb et al. 2013; Ovaskainen et al. 2022).

7. Conclusions

In this study, we examined different remote sensing methods for the multiscale characterisation of brittle structures, ranging from the outcrop scale to the whole of southern Finland. Our analysis included topological, orientation and length distribution properties.

- Connections per branch values were found to vary between 1.85 for the 1:200 000 lineament data and 1.35 for the outcrop fracture networks. Due to the limited size of well-exposed outcrops and the resolution of remote sensing datasets, the topological properties of lineaments remain uncertain.
- The orientation of lineaments is independent of scale, but differences in the orientation of lineaments and outcrop fractures exist. Lineament and fracture orientation is affected by variations in bedrock rheology.
- The determined -1.92 power law exponent for the 1:200 000 lineament dataset is regarded as a good estimate for the length scalability of major lineaments within the Proterozoic bedrock of southern Finland. Uncertainties and biases of the 1:500 000 and full-resolution lineaments cause high uncertainty in estimating the lineament length distribution.
- Outcrop fractures in Kopparnäs follow different length distributions from lineaments and, in addition, are not necessarily described by a single power law exponent. For outcrop fractures of less than 2 m long, a lognormal length distribution was found to provide the only good fit with our data, while the longer ones fitted relatively well with a power law exponent of -2.26.
- A break in data occurs between 100 m and 1 km, where we were unable to map outcrop fractures or lineaments in a statistically consistent way. To better define the boundaries in which, for example, power law length distributions remain valid, sampling of brittle structures from larger, isotropic and less censored outcrop areas is required.

Acknowledgements

This study was funded by Kallioperän rikkonaisuus – Bedrock fracturing project at Geological Survey of Finland, and KYT KARIKKO project, which is a part of the Finnish Research Programme on Nuclear Waste Management (2019-2022). Björn Nyberg, University of Bergen is thanked for advice on two-dimensional fracture network characterization and Markku Paananen, Geological Survey of Finland for advice on aerogeophysical data. Reviewers Phillippe Davy and Billy Andrews, and Editor-in-Chief are thanked for their constructive comments which all helped to improve the manuscript.

References

Aaltonen, I. Engström, J. Front, K. Gehör, S. Kosunen, P. Kärki, A. Mattila, J. Paananen, M. Paulamäki, S. 2016. Geology of Olkiluoto. Posiva Report. Posiva Oy, Eurajoki.

Abdullah, A. Nassr, S. Ghaleeb, A. 2013. Remote Sensing and Geographic Information System for Fault Segments Mapping a Study from Taiz Area, Yemen. Journal of Geological Research 2013, 1–16. https://doi.org/10.1155/2013/201757

Alstott, J. Bullmore, E. Plenz, D. 2014. powerlaw: A Python Package for Analysis of Heavy-Tailed Distributions. In: Rapallo, F. (Ed.), PLoS ONE 9, e85777. https://doi.org/10.1371/journal.pone.0085777

Andrews, B.J. Roberts, J.J. Shipton, Z.K. Bigi, S. Tartarello, M.C. Johnson, G. 2019. How do we see fractures? Quantifying subjective bias in fracture data collection. Solid Earth 10, 487–516. https://doi.org/10.5194/se-10-487-2019

Barton, C.A. Zoback, M.D. Moos, D. 1995. Fluid flow along potentially active faults in crystalline rock. Geology 23, 683–686. https://doi.org/10.1130/0091-7613(1995)023<0683:FFAPAF>2.3.CO;2

Barton, N. Lien, R. Lunde, J. 1974. Engineering classification of rock masses for the design of tunnel support. Rock Mechanics Felsmechanik Mécanique Des Roches 6, 189–236. https://doi.org/10.1007/BF01239496

Bemis, S.P. Micklethwaite, S. Turner, D. James, M.R. Akciz, S. Thiele, S.T. Bangash, H.A. 2014. Ground-based and UAV-Based photogrammetry: A multi-scale, high-resolution mapping tool for structural geology and paleoseismology. Journal of Structural Geology 69, 163–178. https://doi.org/10.1016/j.jsg.2014.10.007

Bense, V.F. Gleeson, T. Loveless, S.E. Bour, O. Scibek, J. 2013. Fault zone hydrogeology. Earth-Science Reviews 127, 171–192. https://doi.org/10.1016/j.earscirev.2013.09.008

Bertrand, L. Géraud, Y. Le Garzic, E. Place, J. Diraison, M. Walter, B. Haffen, S. 2015. A multiscale analysis of a fracture pattern in granite: A case study of the Tamariu granite, Catalunya, Spain. Journal of Structural Geology 78, 52–66. https://doi.org/10.1016/j.jsg.2015.05.013

Bogdanova, S. Gorbatschev, R. Skridlaite, G. Soesoo, A. Taran, L. Kurlovich, D. 2015. Trans-Baltic Palaeoproterozoic correlations towards the reconstruction of supercontinent Columbia/Nuna. Precambrian Research 259, 5–33. https://doi.org/10.1016/j.precamres.2014.11.023

Bond, C.E. Gibbs, D. Shipton, Z.K. 2007. What do you think this is? " Conceptual uncertainty " in geoscience interpretation. Gsa Today 17. https://doi.org/10.1130/GSAT01711A.1

Bonnet, E. Bour, O. Odling, N.E. Davy, P. Main, I. Cowie, P. Berkowitz, B. 2001. Scaling of fracture systems in geological media. Reviews of Geophysics 39, 347–383. https://doi.org/10.1029/1999RG000074

Bossennec, C. Frey, M. Seib, L. Bär, K. Sass, I. 2021. Multiscale Characterisation of Fracture Patterns of a Crystalline Reservoir Analogue. Geosciences 11, 371. https://doi.org/10.3390/geosciences11090371

Boulton, G.S. Dongelmans, P. Punkari, M. Broadgate, M. 2001. Palaeoglaciology of an ice sheet through a glacial cycle:: the European ice sheet through the Weichselian. Quaternary Science Reviews 20, 591–625. https://doi.org/10.1016/S0277-3791(00)00160-8

Bour, O. Davy, P. Darcel, C. Odling, N. 2002. A statistical scaling model for fracture network geometry, with validation on a multiscale mapping of a joint network (Hornelen Basin, Norway). Journal of Geophysical Research: Solid Earth 107, ETG 4-1-ETG 4-12. https://doi.org/10.1029/2001JB000176

Brace, W.F. 1980. Permeability of crystalline and argillaceous rocks. International Journal of Rock Mechanics and Mining Sciences and Geomechanics 17, 241–251. https://doi.org/10.1016/0148-9062(80)90807-4

Ceccato, A. Tartaglia, G. Antonellini, M. Viola, G. 2022. Multiscale lineament analysis and permeability heterogeneity of fractured crystalline basement blocks. Solid Earth 13, 1431–1453. https://doi.org/10.5194/se-13-1431-2022

Chabani, A. Trullenque, G. Ledésert, B.A. Klee, J. 2021. Multiscale Characterization of Fracture Patterns: A Case Study of the Noble Hills Range (Death Valley, CA, USA), Application to Geothermal Reservoirs. Geosciences 11, 280. https://doi.org/10.3390/geosciences11070280

Clauset, A. Shalizi, C.R. Newman, M.E.J. 2009. Power-law distributions in empirical data. SIAM Review 51, 661–703. https://doi.org/10.1137/070710111

Cowie, P.A. 1998. Normal fault growth in three-dimensions in continental and oceanic crust. Washington DC American Geophysical Union Geophysical Monograph Series 106, 325–348. https://doi.org/10.1029/GM106p0325

Cowie, P.A. Scholz, C.H. 1992. Displacement-length scaling relationship for faults: data synthesis and discussion.

Journal of Structural Geology 14, 1149–1156. https://doi.org/10.1016/0191-8141(92)90066-6

Cowie, P.A. Sornette, D. Vanneste, C. 1995. Multifractal scaling properties of a growing fault population. Geophysical Journal International 122, 457–469. https://doi.org/10.1111/j.1365-246X.1995.tb07007.x

Davy, P. Bour, O. De Dreuzy, J.-R. Darcel, C. 2006. Flow in multiscale fractal frac-ture networks. Geological Society, London, Special Publications 261, 31–45. https://doi.org/10.1144/GSL.SP.2006.261.01.03

Davy, P. Le Goc, R. Darcel, C. Bour, O. De Dreuzy, J.R. Munier, R. 2010. A likely universal model of fracture scaling and its consequence for crustal hydromechanics. Journal of Geophysical Research: Solid Earth 115, 1–13. https://doi.org/10.1029/2009JB007043

Davy, Ph. Sornette, A. Sornette, D. 1990. Some consequences of a proposed fractal nature of continental faulting. Nature 348, 56–58. https://doi.org/10.1038/348056a0

Dichiarante, A.M. McCaffrey, K.J.W. Holdsworth, R.E. Bjørnarå, T.I. Dempsey, E.D. 2020. Fracture attribute scaling and connectivity in the Devonian Orcadian Basin with implications for geologically equivalent sub-surface fractured reservoirs. Solid Earth 11, 2221–2244. https://doi.org/10.5194/se-11-2221-2020

Donner, J. 1995. The Quaternary history of Scandinavia. Cambridge University Press, Cambridge.

Ehlers, C. Lindroos, A. Selonen, O. 1993. The late Svecofennian granite-migmatite zone of southern Finland—a belt of transpressive deformation and granite emplacement. Precambrian Research, The Baltic Shield 64, 295–309. https://doi.org/10.1016/0301-9268(93)90083-E

Elminen, T. Airo, M.-L. Niemelä, R. Pajunen, M. Vaarma, M. Wasenius, P. Wennerström, M. 2008. Fault structures in the Helsinki area, southern Finland. Tectonic Evolution of the Svecofennian Crust in Southern Finland - a Basis for Characterizing Bedrock Technical Properties/Pajunen, M. (Ed.). Geological Survey of Finland, Special Paper 47, 185–213, 2008.

EMODnet Bathymetry Consortium, 2018. EMODnet Digital Bathymetry (DTM 2018). https://doi.org/10.12770/18FF0D48-B203-4A65-94A9-5FD8B0EC35F6

Evans, D. Stephenson, M. Shaw, R. 2009. The present and future use of 'land' below ground. Land Use Policy, Land Use Futures 26, S302–S316. https://doi.org/10.1016/j.landusepol.2009.09.015

Follin, S. Hartley, L. Rhén, I. Jackson, P. Joyce, S. Roberts, D. Swift, B. 2014. A methodology to constrain the parameters of a hydrogeological discrete fracture network model for sparsely fractured crystalline rock, exemplified by data from the proposed high-level nuclear waste repository site at Forsmark, Sweden. Hydrogeology Journal 22, 313–331. https://doi.org/10.1007/s10040-013-1080-2

Fox, A. Forchammer, K. Petterson, A. La Pointe, P. Lim, D.-H. 2012. Geological Discrete Fracture Network Model for the Olkiluoto Site, Eurajoki, Finland, Version 2.0. Posiva Report. Posiva Oy, Eurajoki.

Le Garzic, E. de L'Hamaide, T. Diraison, M. Géraud, Y. Sausse, J. de Urreiztieta, M. Hauville, B. Champanhet, J.-M. 2011. Scaling and geometric properties of extensional fracture systems in the proterozoic basement of Yemen. Tectonic interpretation and fluid flow implications. Journal of Structural Geology 33, 519–536. https://doi.org/10.1016/j.jsg.2011.01.012

Geological Survey of Finland, 2020. Spatial data products: Bedrock observations, accessed December 15, 2020, at https://hakku.gtk.fi/en/locations/search?location_id=33.

Glasser, N.F. Roman, M. Holt, T.O. Žebre, M. Patton, H. Hubbard, A.L. 2020. Modification of bedrock surfaces by glacial abrasion and quarrying: Evidence from North Wales. Geomorphology 365, 107283. https://doi.org/10.1016/j.geomorph.2020.107283

Gudmundsson, A. Simmenes, T.H. Larsen, B. Philipp, S.L. 2010. Effects of internal structure and local stresses on fracture propagation, deflection, and arrest in fault zones. Journal of Structural Geology 32, 1643–1655. https://doi.org/10.1016/j.jsg.2009.08.013

Hautaniemi, H. Kurimo, M. Multala, J. Leväniemi, H. Vironmäki, J. 2005. The "Three in One " Aerogeophysical Concept of GTK in 2004. Geological Survey of Finland, Special Paper 39, 21–74, 2005.

Heeremans, M. Wijbrans, J. 1999. Late Proterozoic tectonic events in southern Finland, constrained by40Ar/39Ar incremental heating and single spot fusion experiments on K-feldspars. Terra Nova 11, 216–222. https://doi.org/10.1046/j.1365-3121.1999.00250.x

Henderson, P.J. 1988. Sedimentation in an esker system influenced by bedrock topography near Kingston, Ontario. Canadian Journal of Earth Sciences. https://doi.org/10.1139/e88-098

Hermansson, T. Stephens, M.B. Corfu, F. Page, L.M. Andersson, J. 2008. Migratory tectonic switching, western Svecofennian orogen, central Sweden: Constraints from U/Pb zircon and titanite geochronology. Precambrian Research 161, 250–278. https://doi.org/10.1016/j.precamres.2007.08.008

Hoek, E. Brown, E.T. 1980. Underground excavations in rock, Rev. ed. Institution of Mining and Metallurgy, London.

Huang, N. Jiang, Y. Liu, R. Li, B. Sugimoto, S. 2019. A novel three-dimensional discrete fracture network model for investigating the role of aperture heterogeneity on fluid flow through fractured rock masses. International Journal of Rock Mechanics and Mining Sciences 116, 25–37. https://doi.org/10.1016/j.ijrmms.2019.03.014

Hudson, J.A. Cosgrove, J.W. Kemppainen, K. Johansson, E. 2011. Faults in crystalline rock and the estimation of their mechanical properties at the Olkiluoto site, western Finland. Engineering Geology 117, 246–258. https://doi.org/10.1016/j.enggeo.2010.11.004

James, M.R. 2017. SfM-MVS PhotoScan image processing exercise [WWW Document], ResearchGate. URL https://www.researchgate.net/publication/320407992_SfM-MVS_PhotoScan_image_processing_exercise (accessed 5.20.20)

James, M.R. Chandler, J.H. Eltner, A. Fraser, C. Miller, P.E. Mills, J.P. Noble, T. Robson, S. Lane, S.N. 2019. Guidelines on the use of structure-from-motion photogrammetry in geomorphic research. Earth Surface Processes and Landforms 44, 2081–2084. https://doi.org/10.1002/esp.4637

Jennes, J. 2013. DEM surface tools. Jenness enterprises. Available at: http:// www.jennessent.com/arcgis/surface_area.htm.

Kara, J. Leskelä, T. Väisänen, M. Skyttä, P. Lahaye, Y. Tiainen, M. Leväniemi, H. 2021. Early Svecofennian rift-related magmatism: Geochemistry, U-Pb-Hf zircon isotope data and tectonic setting of the Au-hosting Uunimäki gabbro, SW Finland. Precambrian Research 364, 106364. https://doi.org/10.1016/j.precamres.2021.106364

Kara, J. Väisänen, M. O'brien, H. 2022. Zircon dating of the basalt and felsic dyke in Haveri, SW Finland. Bulletin of the Geological Society of Finland 94, 109–118. https://doi.org/10.17741/bgsf/94.2.001

Kleman, J. Stroeven, A.P. Lundqvist, J. 2008. Patterns of Quaternary ice sheet erosion and deposition in Fennoscandia and a theoretical framework for explanation. Geomorphology, Glacial Landscape Evolution - Implications for Glacial Processes, Patterns and Reconstructions 97, 73–90. https://doi.org/10.1016/j.geomorph.2007.02.049

Korja, A. Heikkinen, P. Aaro, S. 2001. Crustal structure of the northern Baltic Sea palaeorift. Tectonophysics 331, 341–358. https://doi.org/10.1016/S0040-1951(00)00290-0

Kosunen, P. 1999. The rapakivi granite plutons of Bodom and Obbnäs, southern Finland: petrography and geochemistry. Bulletin of the Geological Society of Finland 71, 275–304. https://doi.org/10.17741/bgsf/71.2.005

Krabbendam, M. Bradwell, T. 2014. Quaternary evolution of glaciated gneiss terrains: pre-glacial weathering vs. glacial erosion. Quaternary Science Reviews 95, 20–42. https://doi.org/10.1016/j.quascirev.2014.03.013

Lahtinen, R. Korja, A. Nironen, M. 2005. Chapter 11 Paleoproterozoic tectonic evolution. Developments in Precambrian Geology. Elsevier, 481–531. https://doi.org/10.1016/S0166-2635(05)80012-X

Lahtinen, R. Korja, A. Nironen, M. Heikkinen, P. 2009. Palaeoproterozoic accretionary processes in Fennoscandia. Geological Society, London, Special Publications 318, 237–256. https://doi.org/10.1144/SP318.8

Laitala, M. 1961. Suomen geologinen kartta = geological map of Finland; 1:100 000: Lehti - Sheet 2032. Siuntio: kallioperäkartan selitys = Explanation to the map of rocks. In Finnish. Geologinen tutkimuslaitos, Helsinki.

Maerten, L. Gillespie, P. Pollard, D.D. 2002. Effects of local stress perturbation on secondary fault development. Journal of Structural Geology 24, 145–153. https://doi.org/10.1016/S0191-8141(01)00054-2

Manzocchi, T. 2002. The connectivity of two-dimensional networks of spatially correlated fractures. Water Resources Research 38, 1-1-1–20. https://doi.org/10.1029/2000WR000180

Mattila, J. Viola, G. 2014. New constraints on 1.7 Gyr of brittle tectonic evolution in southwestern Finland derived from a structural study at the site of a potential nuclear waste repository (Olkiluoto Island). Journal of Structural Geology 67, 50–74. https://doi.org/10.1016/j.jsg.2014.07.003

Mauldon, M. 1998. Estimating Mean Fracture Trace Length and Density from Observations in Convex Windows. Rock Mechanics and Rock Engineering 31, 201–216. https://doi.org/10.1007/s006030050021

Mauldon, M. Dunne, W.M. Rohrbaugh, M.B. 2001. Circular scanlines and circular windows: new tools for characterizing the geometry of fracture traces. Journal of Structural Geology 23, 247–258. https://doi.org/10.1016/S0191-8141(00)00094-8

Meixner, J. Grimmer, J.C. Becker, A. Schill, E. Kohl, T. 2018. Comparison of different digital elevation models and satellite imagery for lineament analysis: Implications for identification and spatial arrangement of fault zones in crystalline basement rocks of the southern Black Forest (Germany). Journal of Structural Geology, Spatial Arrangement of Fractures and Faults 108, 256–268. https://doi.org/10.1016/j.jsg.2017.11.006

Mi, L. Jiang, H. Li, J. Li, T. Tian, Y. 2014. The investigation of fracture aperture effect on shale gas transport using discrete fracture model. Journal of Natural Gas Science and Engineering 21, 631–635. https://doi.org/10.1016/j.jngse.2014.09.029

Middleton, M. Schnur, T. Sorjonen-Ward, P. 2015. Geological lineament interpretation using the object-based image analysis approach: results of semi-automated analyses versus visual interpretation. Geological Survey of F1inland, Special Paper 57, 135–154, 20 p.

Miller, R.B. Paterson, S.R. 2001. Influence of lithological heterogeneity, mechanical anisotropy, and magmatism on the rheology of an arc, North Cascades, Washington. Tectonophysics, Partial Melting of Crust and Flow of Orogens 342, 351–370. https://doi.org/10.1016/S0040-1951(01)00170-6

Munier, R. Talbot, C.J. 1993. Segmentation, fragmentation and jostling of cratonic basement in and near Äspö, southeast Sweden. Tectonics 12, 713–727. https://doi.org/10.1029/92TC02722

Neuendorf, K.K.E. Mehl, J.P.J. Jackson, J.A. 2011. Glossary of geology. 5th, rev.

Nironen, M. 1997. The Svecofennian Orogen: A tectonic model. Precambrian Research 86, 21–44. https://doi.org/10.1016/S0301-9268(97)00039-9

Nordbäck, N. 2014. Tunnel Crosscutting Fractures (TCF) in ONKALO (chainage 0-4986). Posiva Working report. No. 2014–58.

Nordbäck, N. Mattila, J. Zwingmann, H. Viola, G. 2022. Precambrian fault reactivation revealed by structural and K-Ar geochronological data from the spent nuclear fuel repository in Olkiluoto, southwestern Finland. Tectonophysics 229208. https://doi.org/10.1016/j.tecto.2022.229208

Nordqvist, A.W. Tsang, Y.W. Tsang, C.F. Dverstorp, B. Andersson, J. 1992. A variable aperture fracture network model for flow and transport in fractured rocks. Water Resources Research 28, 1703–1713. https://doi.org/10.1029/92WR00216

Nyberg, B. Nixon, C.W. Sanderson, D.J. 2018. NetworkGT: A GIS tool for geometric and topological analysis of two-dimensional fracture networks. Geosphere 14, 1618–1634. https://doi.org/10.1130/GES01595.1

Odling, N.E. 1997. Scaling and connectivity of joint systems in sandstones from western Norway. Journal of Structural Geology 19, 1257–1271. https://doi.org/10.1016/S0191-8141(97)00041-2

Odling, N.E. Gillespie, P. Bourgine, B. Castaing, C. Chiles, J.P. Christensen, N.P. Fillion, E. Genter, A. Olsen, C. Thrane, L. Trice, R. Aarseth, E. Walsh, J.J. Watterson, J. 1999. Variations in fracture system geometry and their implications for fluid flow in fractures hydrocarbon reservoirs. Petroleum Geoscience 5, 373–384. https://doi.org/10.1144/petgeo.5.4.373

Ojala, A.E.K. Palmu, J.P. \AAberg, A. \AAberg, S. Virkki, H. 2013. Development of an ancient shoreline database to reconstruct the Litorina Sea maximum extension and the highest shoreline of the Baltic Sea basin in Finland. Bulletin of the Geological Society of Finland 85, 127–144. https://doi.org/10.17741/bgsf/85.2.002

O'Leary, D.W. Friedman, J.D. Pohn, H.A. 1976. Lineament, linear, lineation: Some proposed new standards for old terms. Geological Society of America Bulletin 87, 1463. https://doi.org/10.1130/0016-7606(1976)87<1463:LLLSPN>2.0.CO;2

Ovaskainen, N. 2020. Scalability of lineament and fracture networks within the crystalline Wiborg Rapakivi Batholith, SE Finland. Master's thesis. University of Turku.

Ovaskainen, N. Nordbäck, N. Skyttä, P. Engström, J. 2022. A new subsampling methodology to optimize the characterization of two-dimensional bedrock fracture networks. Journal of Structural Geology 155, 104528. https://doi.org/10.1016/j.jsg.2022.104528

Paananen, M. 2013. Completed Lineament Interpretation of the Olkiluoto Region. Posiva Report No. 2013–02. Eurajoki.

Pajunen, M. Airo, M.-L. Elminen, T. Mänttäri, I. Niemelä, R. Vaarma, M. Wasenius, P. Wennerström, M. 2008. Tectonic evolution of the Svecofennian crust in southern Finland. Tectonic Evolution of the Svecofennian Crust in Southern Finland - a Basis for Characterizing Bedrock Technical Properties/Pajunen, M. (Ed.). Geological Survey of Finland, Special Paper 47, 2008.

Palacios, D. Hughes, P.D. Ruiz, J.M.G. Andrés, N. 2021. European glacial landscapes: maximum extent of glaciations. Elsevier, Amsterdam, 528 pp.

Palmu, J.-P. Ojala, A.E. Ruskeeniemi, T. Sutinen, R. Mattila, J. 2015. LiDAR DEM detection and classification of postglacial faults and seismically-induced landforms in Finland: a paleoseismic database. GFF 137, 344–352. https://doi.org/10.1080/11035897.2015.1068370

Peacock, D.C.P. Nixon, C.W. Rotevatn, A. Sanderson, D.J. Zuluaga, L.F. 2017. Interacting faults. Journal of Structural Geology 97, 1–22. https://doi.org/10.1016/j.jsg.2017.02.008

Peacock, D.C.P. Nixon, C.W. Rotevatn, A. Sanderson, D.J. Zuluaga, L.F. 2016. Glossary of fault and other fracture networks. Journal of Structural Geology 92, 12–29. https://doi.org/10.1016/j.jsg.2016.09.008

Peacock, D.C.P. Sanderson, D.J. 2018. Structural analyses and fracture network characterisation: Seven pillars of wisdom. Earth-Science Reviews 184, 13–28. https://doi.org/10.1016/j.earscirev.2018.06.006

Peacock, D.C.P. Sanderson, D.J. Rotevatn, A. 2018. Relationships between fractures. Journal of Structural Geology 106, 41–53. https://doi.org/10.1016/j.jsg.2017.11.010

Ploegsma, M. Westra, L. 1990. The Early Proterozoic Orijärvi triangle (southwest Finland): a key area on the tectonic evolution of the Svecofennides. Precambrian Research 47, 51–69. https://doi.org/10.1016/0301-9268(90)90030-T

Punkari, M. 1997. Glacial and glaciofluvial deposits in the interlobate areas of the Scandinavian ice sheet. Quaternary Science Reviews, Ice-Contact Sedimentation: Processes and Deposits 16, 741–753. https://doi.org/10.1016/S0277-3791(97)00020-6

Putkinen, N. Eyles, N. Putkinen, S. Ojala, A.E.K. Palmu, J.-P. Sarala, P. Väänänen, T. Räisänen, J. Saarelainen, J. Ahtonen, N. Rönty, H. Kiiskinen, A. Rauhaniemi, T. Tervo, T. 2017. High-resolution LiDAR mapping of glacial landforms and ice stream lobes in Finland. Bulletin of the Geological Society of Finland 89, 64–81. https://doi.org/10.17741/bgsf/89.2.001

Rämö, O.T. Haapala, I. 2005. Chapter 12 Rapakivi Granites. In: Lehtinen, M. Nurmi, P.A. Rämö, O.T. (Eds.), Developments in Precambrian Geology, Precambrian Geology of Finland Key to the Evolution of the Fennoscandian Shield. Elsevier, 533–562. https://doi.org/10.1016/S0166-2635(05)80013-1

Rämö, O.T. Mänttäri, I. 2015. Geochronology of the Suomenniemi rapakivi granite complex revisited: Implications of point-specific errors on zircon U-Pb and refined λ_{87} on whole-rock Rb-Sr. Bulletin of the Geological Society of Finland 87, 25–45. https://doi.org/10.17741/bgsf/87.1.002

Repo, R. Valovirta, V. Rainio, H. 1970. Geological map of Finland 1:100 000; Explanation to the map of Quaternary deposits. Sheet 2032 Espoo (in Finnish). Geological Survey of Finland, Espoo.

Sakaguchi, I. 2017. Emplacement conditions and wallrock reactions of pegmatitic granitoid dikes, Kopparnäs, SW Finland. Master's thesis. University of Helsinki.

Sallasmaa, O. Ahonen, J. Palmu, J-P. Putkinen, N. 2016. Thickness of Superficial deposits in Finland. Bulletin of the Geological Society of Finland, Special Volume 1, 32nd Nordic Geological Winter Meeting – Abstracts, 240-241.

Sanderson, D.J. Nixon, C.W. 2018. Topology, connectivity and percolation in fracture networks. Journal of Structural Geology 115, 167–177. https://doi.org/10.1016/j.jsg.2018.07.011

Sanderson, D.J. Nixon, C.W. 2015. The use of topology in fracture network characterization. Journal of Structural Geology 72, 55–66. https://doi.org/10.1016/j.jsg.2015.01.005

Sanderson, D.J. Peacock, D.C.P. 2020. Making rose diagrams fit-for-purpose. Earth-Science Reviews 201, 103055. https://doi.org/10.1016/j.earscirev.2019.103055

Scheiber, T. Fredin, O. Viola, G. Jarna, A. Gasser, D. Łapińska-Viola, R. 2015. Manual extraction of bedrock lineaments from high-resolution LiDAR data: methodological bias and human perception. GFF 137, 362–372. https://doi.org/10.1080/11035897.2015.1085434

Schlische, R.W. Young, S.S. Ackermann, R.V. Gupta, A. 1996. Geometry and scaling relations of a population of very small rift: related normal faults. Geology 24, 683–686. https://doi.org/10.1130/0091-7613(1996)024<0683:GASROA>2.3.CO;2

Scott, D.N. Wohl, E.E. 2018. Bedrock fracture influences on geomorphic process and form across process domains and scales. Earth Surface Processes and Landforms 44, 27–45. https://doi.org/10.1002/esp.4473

Segall, P. Pollard, D.D. 1983. Joint formation in granitic rock of the Sierra Nevada. GSA Bulletin 94, 563–575. https://doi.org/10.1130/0016-7606(1983)94<563:JFIGRO>2.0.CO;2

Skyttä, P. Mänttäri, I. 2008. Structural setting of late Svecofennian granites and pegmatites in Uusimaa Belt, SW Finland: Age constraints and implications for crustal evolution. Precambrian Research 164, 86–109. https://doi.org/10.1016/j.precamres.2008.04.001

Skyttä, P. Ovaskainen, N. Nordbäck, N. Engström, J. Mattila, J. 2021. Fault-induced mechanical anisotropy and its effects on fracture patterns in crystalline rocks. Journal of Structural Geology 146, 104304. https://doi.org/10.1016/j.jsg.2021.104304

Skyttä, P. Torvela, T. 2018. Brittle reactivation of ductile precursor structures: The role of incomplete structural transposition at a nuclear waste disposal site, Olkiluoto, Finland. Journal of Structural Geology 116, 253–259. https://doi.org/10.1016/j.jsg.2018.06.009

Skyttä, P. Väisänen, M. Mänttäri, I. 2006. Preservation of Palaeoproterozoic early Svecofennian structures in the Orijärvi area, SW Finland—Evidence for polyphase strain partitioning. Precambrian Research 150, 153–172. https://doi.org/10.1016/j.precamres.2006.07.005

Soliman, A. Han, L. 2019. Effects of vertical accuracy of digital elevation model (DEM) data on automatic lineaments extraction from shaded DEM. Advances in Space Research 64, 603–622. https://doi.org/10.1016/j.asr.2019.05.009

van Staal, C.R. Williams, P.F. 1983. Evolution of a Svecofennian-mantled gneiss dome in SW Finland, with evidence for thrusting. Precambrian Research 21, 101–128. https://doi.org/10.1016/0301-9268(83)90007-4

Stroeven, A.P. Hättestrand, C. Kleman, J. Heyman, J. Fabel, D. Fredin, O. Goodfellow, B.W. Harbor, J.M. Jansen, J.D. Olsen, L. Caffee, M.W. Fink, D. Lundqvist, J. Rosqvist, G.C. Strömberg, B. Jansson, K.N. 2016. Deglaciation of Fennoscandia. Quaternary Science Reviews, Special Issue: PAST Gateways (Palaeo-Arctic Spatial and Temporal Gateways) 147, 91–121. https://doi.org/10.1016/j.quascirev.2015.09.016

Tchalenko, J.S. 1970. Similarities between Shear Zones of Different Magnitudes. GSA Bulletin 81, 1625–1640. https://doi.org/10.1130/0016-7606(1970)81[1625:SBSZOD]2.0.CO;2

Thiele, S.T. Jessell, M.W. Lindsay, M. Ogarko, V. Wellmann, J.F. Pakyuz-Charrier, E. 2016. The topology of geology 1: Topological analysis. Journal of Structural Geology 91, 27–38. https://doi.org/10.1016/j.jsg.2016.08.009

Torvela, T. Kurhila, M. 2020. How does orogenic crust deform? Evidence of crustal-scale competent behaviour within the partially molten middle crust during orogenic compression. Precambrian Research 342, 105670. https://doi.org/10.1016/j.precamres.2020.105670

Torvela, T. Kurhila, M. 2022. Timing of syn-orogenic, high-grade transtensional shear zone formation in the West Uusimaa Complex, Finland. Bulletin of the Geological Society of Finland 94, 5-22. https://doi.org/10.17741/bgsf/94.1.001

Torvela, T. Mänttäri, I. Hermansson, T. 2008. Timing of deformation phases within the South Finland shear zone, SW Finland. Precambrian Research 160, 277–298. https://doi.org/10.1016/j.precamres.2007.08.002

Väisänen, M. Hölttä, P. 1999. Structural and metamorphic evolution of the Turku migmatite complex, southwestern Finland. Bulletin of the Geological Society of Finland 71, 177–218. https://doi.org/10.17741/bgsf/71.1.009

Väisänen, M. Mänttäri, I. Hölttä, P. 2002. Svecofennian magmatic and metamorphic evolution in southwestern Finland as revealed by U-Pb zircon SIMS geochronology. Precambrian Research 116, 111–127. https://doi.org/10.1016/S0301-9268(02)00019-0

Väisänen, M. Skyttä, P. 2007. Late svecofennian shear zones in southwestern finland. Gff 129, 55–64. https://doi.org/10.1080/11035890701291055

Verduzco, B. Fairhead, J.D. Green, C.M. MacKenzie, C. 2004. New insights into magnetic derivatives for structural mapping. The Leading Edge 23, 116–119. https://doi.org/10.1190/1.1651454

Wennerström, M. Airo, M.-L. Elminen, T. Niemelä, R. Pajunen, M. Vaarma, M. Wasenius, P. 2008. Orientation and properties of jointing in Helsinki area, southern Finland. Tectonic Evolution of the Svecofennian Crust in Southern Finland - a Basis for Characterizing Bedrock Technical Properties/Pajunen, M. (Ed.). Geological Survey of Finland, Special Paper 47, 253–282, 2008.

Zeeb, C. Gomez-Rivas, E. Bons, P.D. Blum, P. 2013. Evaluation of sampling methods for fracture network characterization using outcrops. AAPG Bulletin 97, 1545–1566. https://doi.org/10.1306/02131312042

Zimmerman, R. Main, I. 2004. Hydromechanical Behavior of Fractured Rocks. International Geophysics. Elsevier, 363–421.
https://doi.org/10.1016/S0074-6142(03)80023-2